Phase decomposition in nanocrystalline $Cr_{0.8}Cu_{0.2}$ thin films

J. Chakraborty [a],[*], T.P. Harzer [b], Maria Jazmin Duarte [b], Gerhard Dehm [b]

[a] Materials Engineering Division, National Metallurgical Laboratory, Council of Scientific and Industrial Research, P.O. Burmamines, Jamshedpur 831007, India
[b] Department of Structure and Nano-/Micromechanics of Materials, Max-Planck-Institut für Eisenforschung GmbH, Max-Planck-Strasse 1, Dusseldorf 40237, Germany

ARTICLE INFO

ABSTRACT

Metastable $Cr_{0.8}Cu_{0.2}$ alloy thin films with nominal thickness of 360 nm have been deposited on Si(100) substrate by co-evaporation of Cu and Cr using molecular beam epitaxy (MBE). Phase evolution, microstructure, stress development, and crystallographic texture in $Cr_{0.8}Cu_{0.2}$ thin films have been investigated by X-ray diffraction (XRD), atom probe tomography (APT) and transmission electron microscopy (TEM) combined with energy dispersive X-ray spectroscopy (EDS) during annealing of the films in the temperature range 200–450 °C. X-ray diffraction of the as-deposited thin film shows single phase bcc crystal structure of the film whereas APT observation of fine precipitates in the film matrix due to inherent compositional fluctuation indicates onset of phase separation via spinodal decomposition regime. XRD (in-situ) and APT investigation of 300 °C annealed film reveals that the early stage of phase separation involves localized formation of metastable intermediate bcc precipitate phase having 60 at% Cr and 40 at% Cu approximately (~$Cr_{0.6}Cu_{0.4}$). For longer duration of annealing at temperature ≥350 °C, such metastable bcc precipitates act as heterogeneous nucleation sites for the onset of precipitation of Cu rich fcc Cu(Cr) phase which indicates a change of phase separation mechanism from 'spinodal decomposition' to 'nucleation and growth'. Annealing of the film at temperature ≥400 °C for longer duration leads to the formation of a two phase structure with Cu rich fcc precipitate phase in a Cr rich bcc matrix. Observed phase decomposition is accompanied by significant changes in the microstructure, residual stress and crystallographic texture in the Cr rich bcc film matrix which leads to the minimization of both surface and strain energies and thereby a reduction of total Gibbs free energy of the thin film. Thermodynamic model calculation has been presented in order to understand the nucleation pathway of Cu rich stable fcc Cu(Cr) precipitates via non-classical nucleation of metastable intermediate bcc $Cr_{0.6}Cu_{0.4}$ phase.

© 2021 Elsevier B.V. All rights reserved.

1. Introduction

Cr-Cu alloys are known for their improved mechanical strength relative to pure copper [1,2], excellent oxidation resistance [3] and fairly high electrical conductivity [4]. However, from the equilibrium phase diagram, the Cr-Cu system has very limited solid solubility due to the high positive enthalpy of mixing between Cr and Cu which hinders the study of Cr-Cu alloys over a wide range of compositions [5,6]. In the last decades, considerable efforts have been made to synthesize metastable nanocrystalline Cr-Cu alloys by various non-equilibrium synthesis methods such as mechanical alloying of Cu and Cr powder mixtures [7,8], atomic mixing under non-equilibrium conditions during vapor deposition of Cr-Cu alloy thin films on a cold substrate (vapor quenching) by co-evaporation [9–11] or co-sputtering [12–16,6] of Cu and Cr and by other solid state routes [17,18]. Whereas by 'mechanical alloying', the Cr-Cu solid solution has been possible only for composition up to 20 at% Cu [7,8], by 'vapor deposition' Cr-Cu solid solutions can be obtained over the entire range of chemical compositions [9,10,13,14]. Very recently, Harzer et al. [10] reported solid solubility of Cu and Cr over composition range 4 at% Cr – 93 at% Cr in metastable nanocrystalline Cu-Cr alloy thin films with single phase face-centered cubic (fcc), body-centered cubic (bcc) and also two phase structures. In this context, it is important to note that over the last decades, such metastable alloy thin films have been synthesized over a wide range of chemical compositions for several other binary metallic systems exhibiting a high positive enthalpy of mixing such as Cu-Co [19–23], Cu-Ag [24–26], Cu-Mo [9,27–29], Cu-Fe [29–31]. Kinetically direct deposition of elements from the vapor phase and quenching the vapor on the unheated substrate forms non-equilibrium alloy thin film since

the diffusion of the condensed adatoms on the substrate is essentially prevented at low substrate temperature. For equilibrium-immiscible binary elements, such vapor deposition at low substrate temperature leads to the formation of random solid solution between the elements in the as deposited alloy thin film with much higher Gibbs free energies as compared to equilibrium (i.e. alloy film is thermodynamically metastable). In case of metastable nanocrystalline binary alloy thin films, such higher free energy originates mainly from the increased elastic strain energy (due to large intrinsic films stresses [9,32–39 *and references therein*]), higher interface energies (due to large density of grain boundaries (GB) and other interfaces in the films) and increased surface energies due to reduced crystallite (or grain) sizes (size ~a few nm) in the thin films. Since both crystallite size and film stress are temperature dependent, the total Gibbs free energies and hence the phase stability of these alloy thin films strongly depends on the substrate temperature during film deposition and/or post deposition annealing temperature [11–14,33,34,39–43]. Mader observed decomposition of several metastable crystalline alloy thin films near 0.45 T_m where T_m is the melting point of the respective alloys [33]. In case of Cu rich and Cr rich Cr-Cu alloy films, Shin et al. was the first to find no sign of phase separation after annealing the films at 300 °C for 24 h although some finite degree of phase separation was observed by these authors in Cr rich films annealed at 400 °C for 24 h and in Cu rich films annealed at 450 °C for 0.5 h respectively [12]. In subsequent years, phase stability of metastable Cr-Cu alloy films of various compositions has been examined under isothermal annealing by several researchers [11–14]. A general observation is that the phase separation in metastable Cr-Cu alloy films often involves metastable to equilibrium phase transformation through precipitation of pure second phase (either Cu or Cr) without the formation of any intermediate phase. Observation of intermediate fcc Cr rich precipitates in the Cu rich fcc Cu matrix during the early stage of phase separation of $Cu_{0.9}Cr_{0.1}$ thin films has been reported by McIntyre et al. [3]. Similar observation of fcc Cr rich precipitates has been reported during early stage of annealing of bulk Cu-Cr-Zr alloys in recent years [44]. Despite several reports, a detailed investigation of early stage of phase separation mechanism especially via intermediate phase formation (if any) along with the underlying thermodynamics and kinetics during the post deposition annealing of metastable Cr-Cu alloy thin films is rare whereas phase separation in bulk metastable Cr-Cu alloys has been addressed by several researchers [11,14,32,34,45–55]. Furthermore, phase decomposition in binary alloy thin film may be influenced by the residual stress present in the film matrix (and its variation with temperature) which may change when the molar volume of the precipitate and the matrix differs. Besides residual stress, phase decomposition process in polycrystalline thin alloy film is further complicated by the crystallographic texture often present in the alloy film matrix. Crystallographic orientation relationship between the matrix and the precipitate phase is often controlled by the existing crystallographic orientation of the parent phase in case of both bulk [44,47,48,52,55] and thin film [13,14] Cr-Cu alloys. In view of the above considerations, a detailed phase separation study in Cr-Cu alloy thin films must take into account the stress, texture and microstructure for both matrix and precipitate phases and the related thermodynamics. Such a correlation however, has not been established in Cr-Cu alloy thin films studied so far. In the present work, a detailed experimental investigation of phase decomposition of nanocrystalline $Cr_{0.8}Cu_{0.2}$ alloy thin films during isothermal aging at 200 °C, 300 °C, 350 °C, 400 °C and 450 °C has been reported with a special emphasis to understand the early stage of phase decomposition of the alloy thin films. Attempt has been made to establish a correlation between the observed phase decomposition and associated changes in the microstructure, residual stresses and crystallographic textures in the $Cr_{0.8}Cu_{0.2}$ alloy thin films (and their thermodynamic consequences).

Thermodynamic origin of nucleation pathway of Cu rich fcc Cu(Cr) precipitates in the Cr rich bcc Cr(Cu) matrix has been theoretically investigated.

2. Specimen preparation and characterization

Nanocrystalline $Cr_{0.8}Cu_{0.2}$ alloy thin films (thickness: 358 ± 3 nm) have been deposited on Si (100) wafers coated with a 50 nm thick amorphous Si_3N_4 layer to prevent chemical reactions between the substrate and the $Cr_{0.8}Cu_{0.2}$ alloy film. Film thicknesses were measured by lateral movement of a diamond stylus with constant vertical force across the film/substrate interface using a 'Tencor Alpha-step 200 contact profilometer'. Deposition of alloy thin films was carried out by simultaneous evaporation of the constituent elements from thermal effusion cells in a custom built molecular beam epitaxy (MBE) system operated under ultra-high vacuum condition (nominal pressure ~ 10^{-9} mbar). During film deposition the substrate temperature increased up to 102°C due to radiation heating caused by the temperature of the effusion cells. Detailed overview of the substrate temperature, film thickness and other deposition parameters can be obtained from Table -1 presented in ref. [10]. To estimate the global film composition of the Cr-Cu alloy films, energy dispersive X-ray spectroscopy (EDS) measurements were carried out in a JEOL 6490 scanning electron microscope operated at an acceleration voltage of 15 kV, whereas the local chemical film composition was identified by the EDS measurements performed in a JEOL JEM-2200FS field emission gun transmission electron microscope (TEM) operated at 200 kV and by atom probe tomography (APT). TEM studies of the nanostructure was performed on focused ion beam (FIB) prepared cross-sections of the $Cr_{0.8}Cu_{0.2}$ alloy films using either a 200 kV JEOL JEM-2200FS or a 300 kV FEI Titan Themis field emission gun instrument. Selected area electron diffraction (SAD) patterns for phase identification were acquired at a camera length of 300 mm using a selected area aperture of 20 µm in diameter. APT measurements were carried out in a LEAP™ 3000X HR local electrode atom probe from 'Cameca Instruments' [56–58]. The base temperature was set to 60 K and the measurements were performed in voltage mode at 200 kHz pulse frequency, 15% pulse fraction and 0.5% detection rate. APT specimens of the as-grown and annealed films at 300 °C for 2.5 h were prepared by using a FEI Helios 600i Dual Beam workstation as described elsewhere [59]. As-deposited $Cr_{0.8}Cu_{0.2}$ alloy thin films were characterized both by in-situ (high temperature) and *ex-situ* (room temperature) X-ray diffraction (XRD) using CoK_α radiation in a GE-Seifert theta-theta diffractometer equipped with parallel beam optics (polycapillary), an Eulerian cradle and an energy dispersive x-ray detector (Meteor 0D). The in-situ XRD of as-deposited films was carried out by annealing the films for one hour in nitrogen atmosphere using a high temperature specimen stage (Anton Paar DHS1100). A heating rate of 50 °C/min. was used to reach the final annealing temperatures of 200 °C, 300 °C, 350 °C, 400 °C and 450 °C. The in-situ XRD patterns were recorded in Bragg-Brentano geometry over the angular range of 48° to 55° (2θ) with 0.1° step width and 10 s as time/step for the phase analysis. Furthermore, *ex-situ* XRD of as-deposited and compressed air cooled annealed specimen have been recorded in the Bragg-Brentano geometry over the angular range 30° to 130° (2θ) with 0.05° step width and 10 s as time/step. XRD patterns have been fitted with Pearson-VII functions using two different peak fitting programs ('X'pert High Score Plus' and 'PROFIT', PANAlytical [60,61]) in order to determine the peak parameters namely peak maximum positions, FWHM (full width at half maximum), integral breadth and integrated intensity corresponding to $K\alpha_1$ radiation. Crystallite size and the micro–strain evolution of annealed $Cr_{0.8}Cu_{0.2}$ films were carried out by employing the so-called single-line broadening analysis [62] applied to {110} reflection of the $Cr_{0.8}Cu_{0.2}$ phase. This method of X-ray line profile analysis has been

adopted in view of the textured nature of $Cr_{0.8}Cu_{0.2}$ thin films. Correction of instrumental line broadening has been made by measuring a standard specimen of Si (standard reference material, National Institute of Standards and Technology, Gaithersburg, USA). Detailed formulation of single line analysis method can be obtained from Ref. [62].

As a next step, the same Seifert diffractometer has been used for the *ex-situ* stress measurement of $Cr_{0.8}Cu_{0.2}$ films in the conventional diffraction geometry for the diffraction stress analysis by the $d_{\psi}^{hkl} - sin^2\psi$ method [63]. Macroscopic strain measurements of nanocrystalline $Cr_{0.8}Cu_{0.2}$ films have been performed by measuring orientation dependent inter-planar lattice spacing (d_{ψ}^{hkl}) corresponding to {110} and {220} reflections of the bcc $Cr_{0.8}Cu_{0.2}$ phase at various specimen tilt angles (ψ). Strain measurements performed at both positive and negative specimen tilt angles generated the same $d_{\psi}^{hkl} - sin^2\psi$ plots (i.e. no ψ splitting was observed) which indicates presence of negligible shear stresses in the films. For a rotationally symmetric plane state of stress (measurements at rotation angles $\varphi = 0°$ and $\varphi = 90°$ yield the same stress value $\sigma_{\parallel}$), the stress $\sigma_{\parallel}$ can be determined from the following equation [63]:

$$d_{\psi}^{hkl} = \frac{1}{2} s_2^{hkl} d_0^{hkl} \sigma_{\parallel} sin^2\psi + (1 + 2 s_1^{hkl} \sigma_{\parallel}) d_0^{hkl} \quad (1)$$

where d_0^{hkl} is the strain free lattice spacing of the {hkl} planes. S_1^{hkl} and $(1/2)S_2^{hkl}$ are the so-called X-ray elastic constants [63]. For the nanocrystalline bcc Cr(Cu) phase, Eshelby-Kröner average X-ray elastic constants (S_1^{hkl} and $(1/2)S_2^{hkl}$) and of pure Cr were used with S_1^{hkl} as $- 0.77 \times 10^{-12} Pa^{-1}$ and $(1/2)S_2^{hkl}$ as $4.50 \times 10^{-12} Pa^{-1}$ for {110} (and {220}) bcc reflections [64]. However, due to the presence of a {110} fiber texture of the bcc phase in the $Cr_{0.8}Cu_{0.2}$ thin films (see Section 3.3), the use of the X-ray stress factors would have been a more accurate approach instead of using X-ray elastic constants, which are strictly valid only in the case of untextured specimens exhibiting isotropic grain interactions [65]. From Eq. (1) it can be seen that the stress ($\sigma_{\parallel}$) can be calculated from the slope of the straight line fitted to the data obtained by plotting d_{ψ}^{hkl} versus $sin^2\psi$. Strain free lattice parameters for the as-deposited and annealed $Cr_{0.8}Cu_{0.2}$ films were determined from the d_{ψ}^{hkl}-$sin^2\psi$ plots following a procedure described elsewhere [63,66]. Pole figure measurements ($I(\varphi \psi)$), of {110} reflections of bcc Cr(Cu) phase and {111} reflections of the phase separated fcc Cu(Cr) phase (see Section 3.3) were carried out where I, φ and ψ were the peak maximum intensity, specimen rotation angle and specimen tilt angle, respectively.

3. Results and interpretation

3.1. Phase analysis of $Cr_{0.8}Cu_{0.2}$ films: ex situ and in-situ XRD observations

Fig. 1 shows a representative cross-sectional TEM micrograph of $Cr_{0.8}Cu_{0.2}$ film having thickness 358 ± 3 nm measured by profilometer (see Section 2). The columnar microstructure becomes visible due to the diffraction contrast. Fig. 2(a) shows the XRD patterns corresponding to both as-deposited and annealed nanocrystalline $Cr_{0.8}Cu_{0.2}$ thin films measured *ex-situ*. The prominent Bragg peaks in the XRD patterns of as-deposited and annealed films could be indexed with respect to the bcc structure of Cr where the as-deposited film has the strain free lattice parameters $a = 0.2889 \pm 0.0002$ nm determined from the corresponding d-$sin^2\psi$ plot obtained after stress measurement (see Section 3.4). Lattice parameter of pure bcc Cr phase (bulk value) is 0.2884 nm. The strongest relative peak intensity of the {110} Cr Bragg reflection implies that the $Cr_{0.8}Cu_{0.2}$ film has a preferred {110} orientation. With increasing annealing temperature beyond 350ºC, additional peaks (marked with open and closed rectangles) become visible in the XRD patterns. The relative intensities of these phases grow with
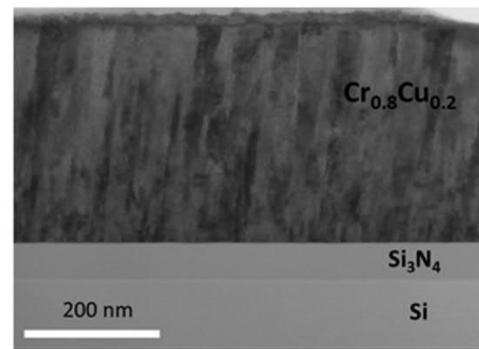

Fig. 1. Cross-sectional TEM micrograph of $Cr_{0.8}Cu_{0.2}$ thin film.

increasing annealing temperature. The new peaks are verified to be neither from the Si-substrate nor from the Cr phase and are indexed with respect to a fcc crystal structure. The lattice parameter calculated from the diffraction peak position of {111} reflection is 0.3611 ± 0.0004 nm which is very close to that of pure fcc Cu phase (bulk value) ~0.3612 nm. This confirms the formation of fcc Cu(Cr) phase in the bcc Cr(Cu) matrix having global chemical composition of $Cr_{0.8}Cu_{0.2}$. The strongest peak of the observed fcc Cu(Cr) phase corresponds to the {111} plane which implies that the fcc phase is also showing a {111} preferred orientation. No other reflection of the fcc phase are noticeably visible except a very weak {200} reflection. Fig. 2(b) shows ratios of integrated intensities ($I_{\{111\}fccCu(Cr)}/I_{\{110\}bccCr(Cu)}$) plotted as function of annealing temperature. The relative integrated intensity of fcc phase after annealing 1 h at the corresponding temperature is found to increase almost exponentially with increasing annealing temperature, suggesting that the fraction of the fcc phase increases with increasing annealing temperature.

Fig. 3(a)-(d) show the XRD patterns measured in-situ in the 2θ range 48° to 55° after 45 min of annealing the $Cr_{0.8}Cu_{0.2}$ films at various temperatures (300–450 °C). Evolution of fcc Cu(Cr) phase with annealing temperature can be clearly discerned from the logarithmic plots of the intensity data with the angle of diffraction (2θ) (see {111} Cu reflection in Fig. 3). Additionally, in case of 300°C annealed films, appearance of a 'shoulder like' diffraction signal between {110} Cr and {111} Cu diffraction peaks (arrows marked in Fig. 3(a) and (b)) indicates formation of a 'less Cr rich' intermediate phase (compared to bcc $Cr_{0.8}Cu_{0.2}$ matrix phase). Such intermediate phase may be crystallographically similar to the bcc Cr(Cu) matrix phase with a different chemical composition than that of the matrix. In case of 350 °C annealed film, presence of two different 'shoulder like' diffraction signals (marked with arrow and circle) implies two different phases indicating possible transition to the Cu rich fcc phase. For annealing at temperature ≥400 °C for 45 min, diffraction signal from the Cr richer intermediate phase gradually disappears and {111} diffraction peak corresponding to the Cr depleted Cu rich fcc Cu(Cr) phase (with lattice parameter close to that of pure Cu) appears in the XRD pattern. Therefore, it seems that the Cr richer intermediate phase was thermodynamically metastable in nature. Additionally, the broadening of {110} bcc Cr(Cu) peak reduces with higher annealing temperature most likely due to annihilation of lattice defects (the grain size of the films do not change significantly with annealing temperature (see Section 3.2 and Fig. 6)). The relative integrated intensity of the fcc Cu(Cr) phase is found to be the highest at 450°C annealing temperature which was earlier observed from the *ex-situ* XRD patterns (Fig. 2(b)). However, a quantitative estimation of volume fraction of fcc Cu(Cr) phase from the in-situ XRD data is difficult especially at 300 °C and 350 °C due to the relatively weak intensity of the {111} fcc Cu(Cr) diffraction peak. Thus, the above in-situ XRD results confirm phase decomposition of $Cr_{0.8}Cu_{0.2}$ thin film through certain intermediate phase formation during
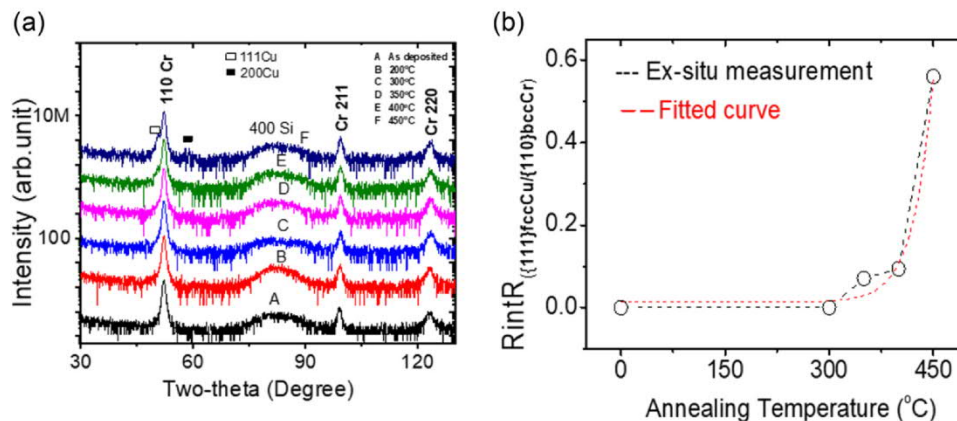
Fig. 2. (a): XRD patterns (*ex-situ*) of $Cr_{0.8}Cu_{0.2}$ thin films. Note: Diffraction patterns are shifted on the logarithmic intensity scale for better visualization and hence the background noise is visible. (b): Ratio of the integrated intensities of {111} fcc Cu and {110} bcc Cr(Cu) peaks (Volume fraction of the fcc Cu(Cr) phase). Error bars are smaller than the sizes of the displayed data circles.

annealing the film at 300 °C and 350 °C and the formation of a two phase structure (fcc Cu(Cr) phase + bcc Cr(Cu) matrix) preferably after the film is annealed at 400 °C and above. Fig. 4(a)-(d) show the evolution of the Cu rich fcc Cu(Cr) phase at 450°C with annealing time recorded during the in-situ XRD measurements. The ratios of integrated intensities ($I_{\{111\}fcc\ Cu(Cr)}/I_{\{110\}Cr(Cu)}$) plotted as function of annealing time for an annealing temperature of 450°C are presented in Fig. 5 which implies that the volume fraction of fcc Cu(Cr) phase increases up to 45 min annealing and beyond which it saturates. Obtained experimental data in Fig. 5 has been fitted with an

analytical fitting function similar to sigmoidal curve (the so called 'S' curve) with reasonable fitting accuracy (see Fig. 5 for the equation of fitted curve). If the 'volume fraction of fcc Cu(Cr) phase' is assumed to be synonymous with the 'transformed phase fraction' (f) of the fcc Cu(Cr) phase in a sense of traditional phase transformation theory, then Fig. 5 can in principle reveal the qualitative mechanism of kinetics of phase decomposition of the $Cr_{0.8}Cu_{0.2}$ alloy thin films. To this end, a plot of $\ln(1/\ln(1-f))$ Vs. $\ln(t)$ (not presented here) has been constructed and it has been observed that the plot follows a straight line behavior with a slope of 3 only for annealing time (t)
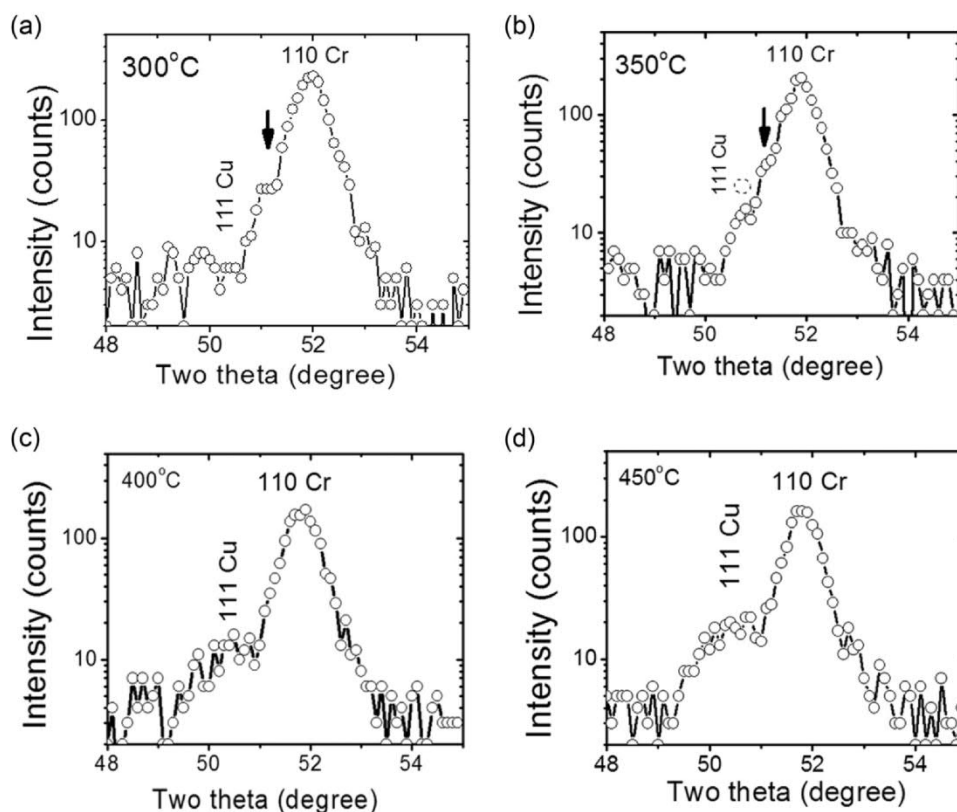

Fig. 3. (a): XRD pattern of 110 bcc Cr(Cu) diffraction peak measured in-situ after 45 min annealing of $Cr_{0.8}Cu_{0.2}$ thin film at 300 °C. Formation of a less Cr rich intermediate phase (see text) is indicated by an arrow. 2θ position of 111 Cu diffraction peak from the Cu rich fcc Cu(Cr) phase is also indicated. (b): XRD pattern of 110 bcc Cr(Cu) diffraction peak measured in-situ after 45 min annealing of $Cr_{0.8}Cu_{0.2}$ thin film at 350 °C. Diffraction signal from a new phase is indicated by circle in addition to the arrow marked Cr richer phase. 2θ position of 111 Cu diffraction peak from the Cu rich fcc Cu(Cr) phase is also indicated. (c): XRD pattern of 110 bcc Cr(Cu) diffraction peak measured in-situ after 45 min annealing of $Cr_{0.8}Cu_{0.2}$ thin film at 400 °C. Appearance of 111 Cu diffraction peak from the Cu rich fcc Cu(Cr) phase with lattice parameter close to that of pure Cu is indicated. (d): XRD pattern of 110 bcc Cr(Cu) diffraction peak measured in-situ after 45 min annealing of $Cr_{0.8}Cu_{0.2}$ thin film at 450 °C. 111 Cu diffraction peak from the Cu rich fcc Cu(Cr) phase having lattice parameter close to that of pure Cu is clearly indicated.
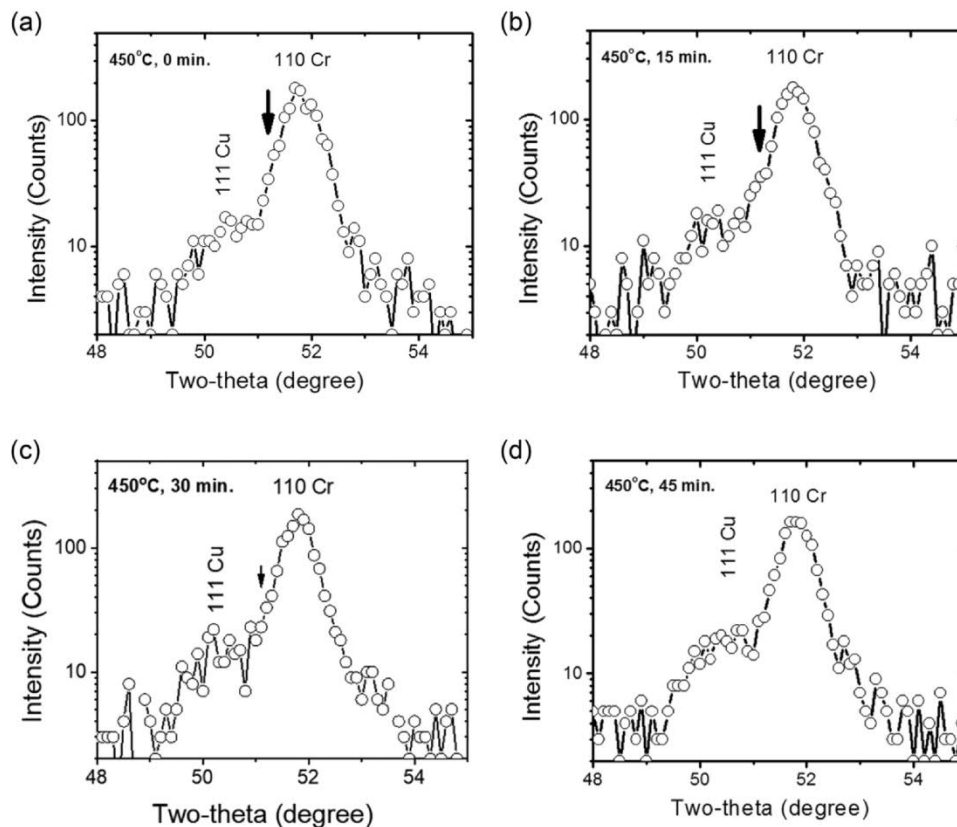
Fig. 4. (a): XRD pattern of 110 bcc Cr(Cu) diffraction peak measured in-situ after annealing the $Cr_{0.8}Cu_{0.2}$ thin film at 450 °C for 0 min. Diffraction signal from the 111 Cu peak of fcc Cu(Cr) phase is shown. 2θ position of the intermediate phase is indicated by the arrow. (b): XRD pattern of 110 bcc Cr(Cu) diffraction peak measured in-situ after annealing the $Cr_{0.8}Cu_{0.2}$ thin film at 450 °C for 15 min. Diffraction signal from the 111 Cu peak of fcc Cu(Cr) phase is shown. 2θ position of the intermediate phase is indicated by the arrow. (c): XRD pattern of 110 bcc Cr(Cu) diffraction peak measured in-situ after annealing the $Cr_{0.8}Cu_{0.2}$ thin film at 450 °C for 30 min. Diffraction signal from the 111 Cu peak of fcc Cu(Cr) phase is shown. 2θ position of the intermediate phase is indicated by the arrow. (d): XRD pattern of 110 bcc Cr(Cu) diffraction peak measured in-situ after annealing the $Cr_{0.8}Cu_{0.2}$ thin film at 450 °C for 45 min. Diffraction signal from the 111 Cu peak of fcc Cu(Cr) phase is shown.
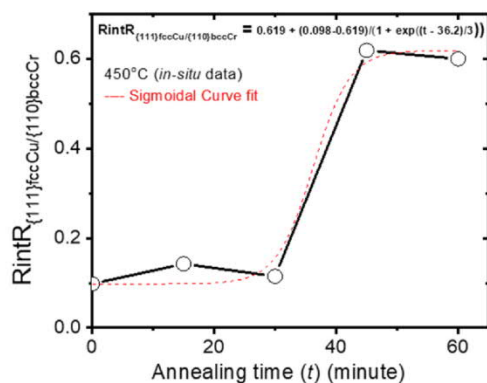

Fig. 5. Time evolution of Cu phase at 450 °C annealing temperature: Ratio of the integrated intensities of {111} fcc Cu(Cr) peak and {110} bcc Cr(Cu) peak measured by in-situ XRD at 450 °C. Error bars are smaller than the sizes of the displayed data circles.

longer than 30 min and not for the entire range of annealing duration used in the present work. This indicates that the formation and growth of the fcc Cu(Cr) phase follows the traditional Johnson-Mehl-Avrami-Kolomogorov (JMAK) empirical law [67] with time exponent 3 for annealing duration > 30 min. For shorter annealing duration (0–30 min), the kinetics of fcc Cu(Cr) phase precipitation is influenced by the presence of the 'less Cr rich' metastable intermediate phase in the bcc Cr(Cu) matrix (see arrow marked diffraction signal in Fig. 4(b) for 450 °C, 15 min annealed thin film for the evidence of such intermediate phase and see Section 4.1 for detailed discussion). Evidence of such intermediate phase formation has also been

confirmed for 300 °C and 350 °C annealed thin films (arrow marked diffraction signals in Fig. 3(a) and (b)).

3.2. Microstructure of $Cr_{0.8}Cu_{0.2}$ films: XRD, TEM and APT observations

Average crystallite size (size of the coherently diffracting domains) in the $Cr_{0.8}Cu_{0.2}$ thin films plotted with annealing temperature shows an initial size increase from 40 ± 6 nm up to 55 ± 9 nm at 200 °C (see Fig. 6(a)). Surprisingly, further increase of annealing temperature leads to negligible change in crystallite size except some noticeable data scatter at 350 °C and 450 °C annealing temperature. Interestingly, the microstrain (inhomogeneous) in the $Cr_{0.8}Cu_{0.2}$ films decreases with increasing annealing temperature (Fig. 6(b)) due to annihilation of lattice defects in the bcc Cr(Cu) matrix. At 450 °C annealing temperature, the microstrain in the $Cr_{0.8}Cu_{0.2}$ thin films is reduced by almost 20% as compared to the as-grown film (Fig. 6(b)). It may be noted that great care has been taken in the fitting of XRD pattern and the data analysis (described in Section 2), however, diffraction line broadening analysis by single line method may involve large systematic errors whose estimation is not straightforward [62]. In the present work, statistical error in the value of the integral breadth has been estimated by various possible data fitting of the XRD pattern which has led to an uncertainty of ~15% in the volume averaged crystallite size and ~10% for the microstrain. STEM-EDS analysis of elemental distribution of Cu and Cr inside the as-deposited $Cr_{0.8}Cu_{0.2}$ thin film has been published elsewhere [10]. Additionally, the local composition and microstructure of the as-deposited thin film and a film annealed at 300 °C for 2.5 h was evaluated also by APT. Although for the as-grown film,
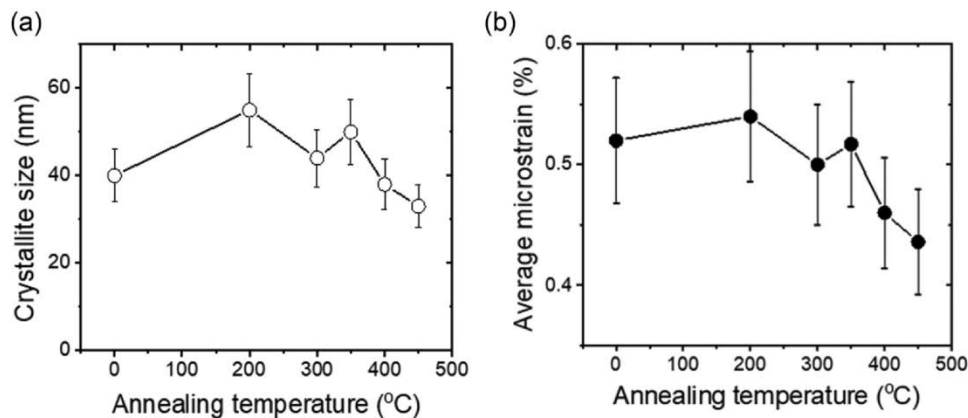
Fig. 6. (a): Average crystallite size in the $Cr_{0.8}Cu_{0.2}$ thin film plotted as a function of annealing temperature. (b): Average microstrain in the $Cr_{0.8}Cu_{0.2}$ thin film plotted as a function of annealing temperature.

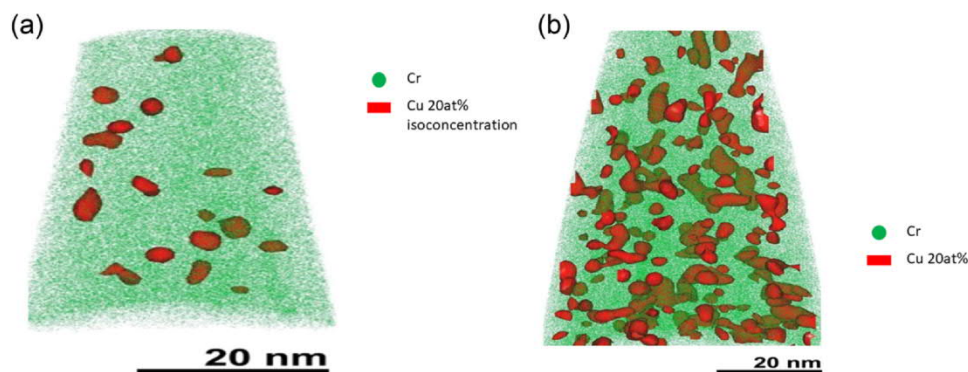**Fig. 7.** (a): APT reconstruction of as deposited $Cr_{0.8}Cu_{0.2}$ thin films showing fine precipitates (average diameter: 3 ± 0.4 nm). The Cu threshold for iso-concentration surfaces was chosen as 20 at%. (b): As deposited thin films annealed at 300 °C for 2.5 h showing precipitates of different morphologies. An isoconcentration surface of 20 at% Cu is in red color.

neither by TEM nor by XRD the presence of the fcc Cu phase was detected, APT reconstructions show fine precipitates with an average diameter of 3 ± 0.4 nm and compositions of 68.5 ± 6 at% Cr and 31.5 ± 6 at% Cu (Fig. 7a). As the film is annealed at 300 °C for 2.5 h these clusters grow only slightly to 3.5 ± 0.4 nm, but their average Cu content increases by more than 10 at% to 43.2 ± 5 at% (Fig. 7b).

Annealing the film at 300 °C for ~2.5 h results in precipitates of different sizes and morphologies (mainly sphere, ellipsoid and plate shaped) and Cu concentrations (shown in red color in Fig. 7(b)). It seems that some of these precipitates coalesce with each other. In addition, strong signals of CrO^+ ions are observed after annealing. In Fig. 8(a) it can be observed that CrO^+ ions are accumulated in plate
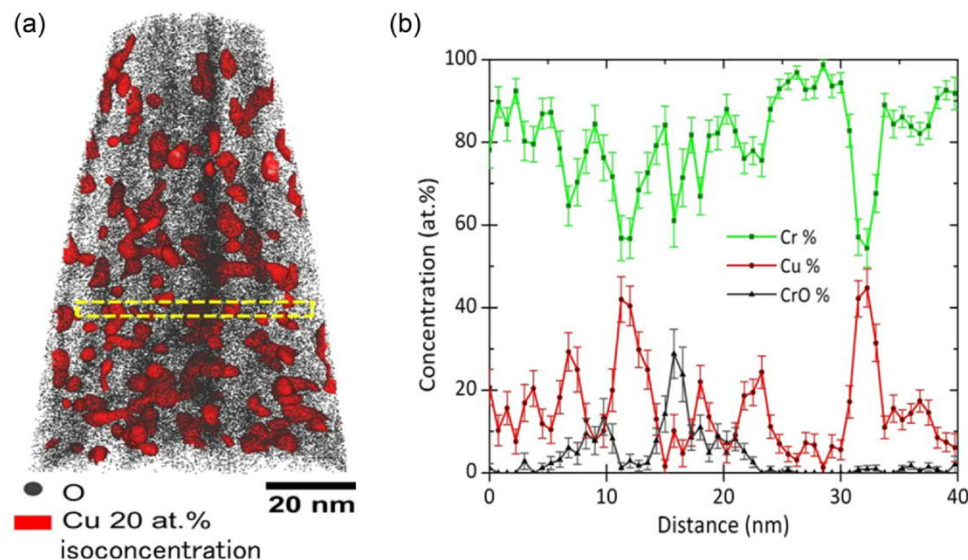

Fig. 8. (a): APT reconstruction of 300 °C, 2.5 h annealed thin films showing Cu rich precipitate phase. Yellow dashed region is marked for measurements of concentration profiles presented in (b). The Cu threshold for iso-concentration surfaces was chosen as 20 at%. (b): Measured concentration profiles of Cr, Cu and CrO from the yellow dashed region shown in the APT image presented in (a).

shaped regions parallel to the evaporation direction, following the columnar growth of the film. This suggests that possibly oxides formed at the columnar grain boundaries (GBs) during annealing. A cylindrical volume of 3 nm diameter and 40 nm long was extracted in the region highlighted by the yellow dashed line of Fig. 8(a), crossing different regions. In the concentration profile of Fig. 8(b), corresponding to the extracted volume, a Cu-rich region can be seen in the vicinity of the CrO^+ signal which indicates that the Cu-rich precipitates form adjacent to the GB regions (note: average crystallite size/mean GB spacing ~ 40 nm). It is known from the earlier work on similar Cu-Cr thin films that the oxygen (if present) usually accumulates at the GBs [68]. However, Cu rich precipitates also form inside the grains within the matrix, as suggested by the second Cu-rich region in the same concentration profile and other Cu peaks of lower concentrations (see Fig. 8(b)).

In addition to the conducted XRD and APT measurements, TEM was also performed on a few selected alloy films after annealing for 60 min at 300 °C and 450 °C. SAD combined with STEM-EDS reveals the presence of the fcc Cu(Cr) phase in the 450 °C annealed thin films. The SAD pattern of Fig. 9(a) shows the presence of weak fcc Cu {200}, {220} and {311} Bragg reflections (Fig. 9(b)), whereas a discrimination between the fcc Cu {111} and bcc Cr {110} Bragg reflection is not possible due to similar lattice plane distances. Besides the bcc Cr and fcc Cu Bragg reflections, also some weak oxide related reflections (e.g. Cr_2O_3 and CuO) are observed in the SAD pattern which are most likely caused either by surface oxidation of the constituent elements during TEM sample preparation and storage or due to residual oxygen during annealing of the films. The STEM-EDS measurements of Fig. 9(a) show 14 ± 4 nm sized Cu enriched film areas which are located at the columnar GBs (Fig. 9(c)) and contain 41 ± 8 at% Cu demonstrating the ongoing phase separation of the alloy film. It should be noted that the acquired EDS-maps (Fig. 9(c)) are a two dimensional (2D) projection of the actual elemental distribution in the TEM sample along the beam direction. Thus, in case of overlapping fcc Cu(Cr) precipitates and Cr(Cu) matrix regions, their signals will be mixed.

3.3. Texture evolution in $Cr_{0.8}Cu_{0.2}$ films

Fig. 10(a)-(f) show fiber textures in the measured pole figures corresponding to $\{110\}_{bcc}$ reflections of bcc Cr(Cu) phase in the as-deposited and annealed $Cr_{0.8}Cu_{0.2}$ thin films. In case of fiber texture, intensity is independent of specimen rotation angle φ, and hence complete texture information can be obtained from the pole figure cut which is the plot of intensity at various specimen tilt angles (ψ) at a fixed specimen rotation angle (φ). Such fiber plots are presented in Fig. 10(g) corresponding to {110} Cr reflection of bcc Cr(Cu) phase. For the as-deposited and annealed $Cr_{0.8}Cu_{0.2}$ films, pole figure

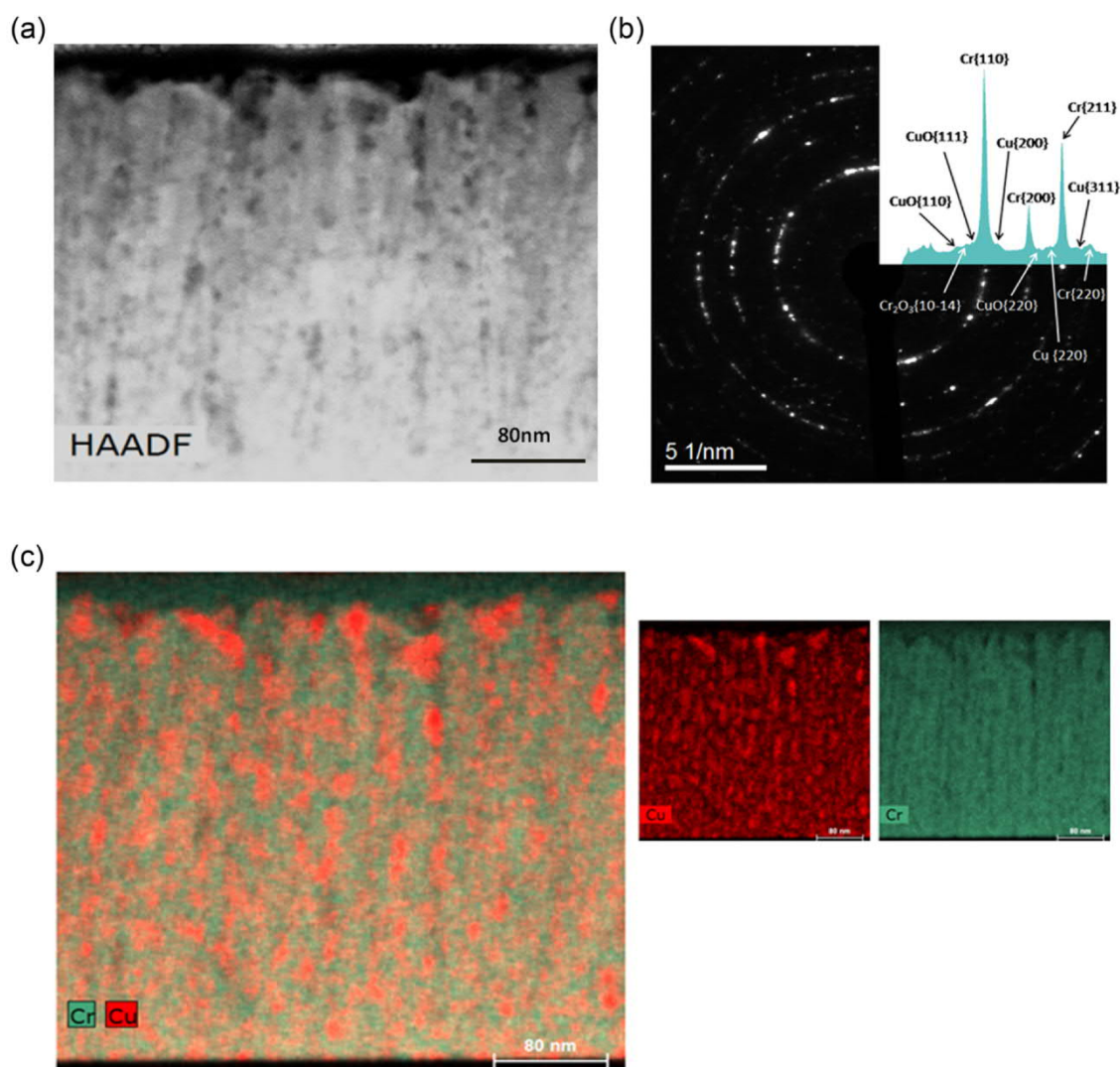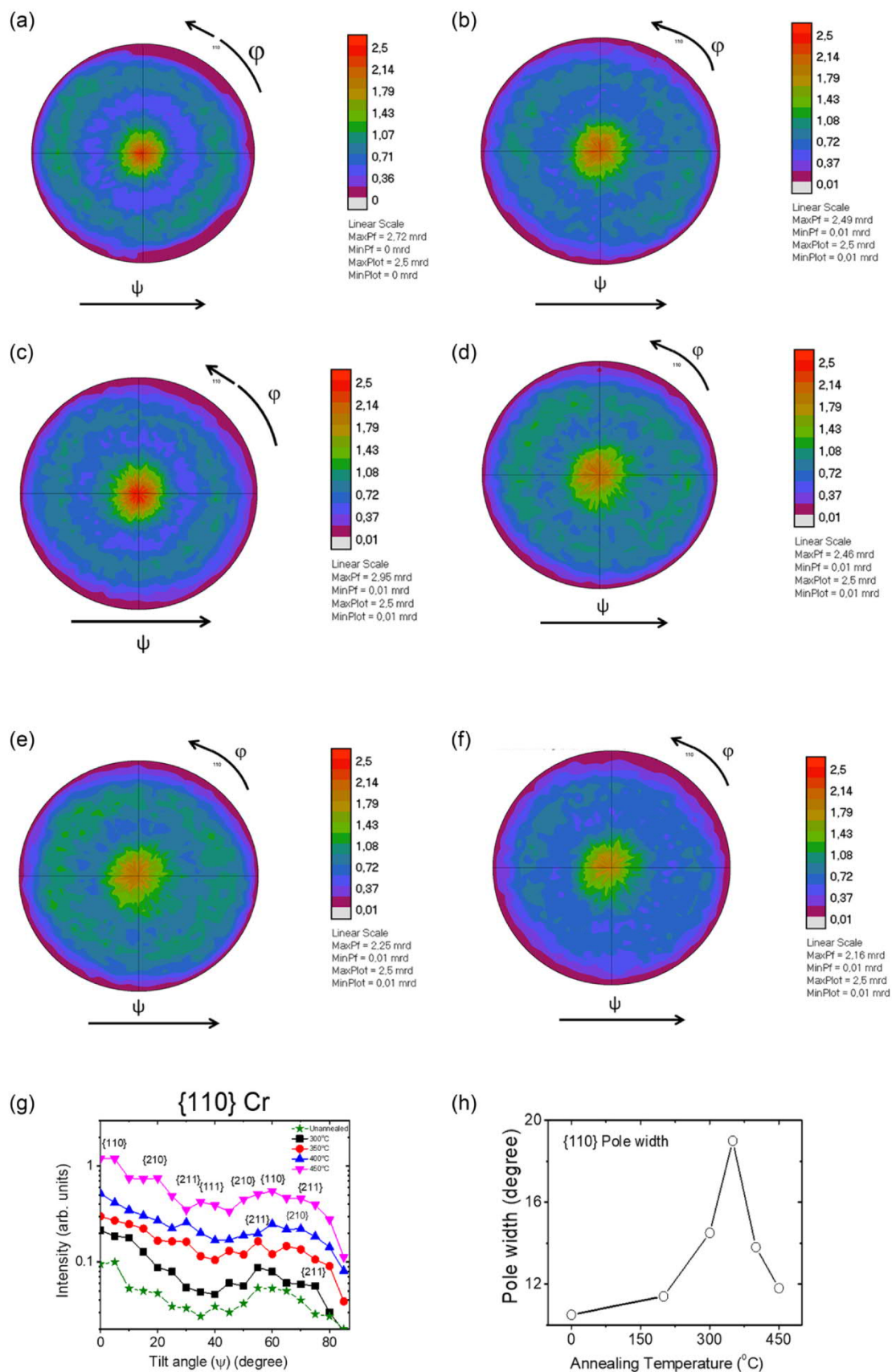**Fig. 9.** (a) STEM (HAADF) image of $Cr_{0.8}Cu_{0.2}$ thin film annealed at 450 °C for 1 h. (b): SAD pattern taken from (a). (c): STEM-EDS measurement of (a); STEM-EDS map shows elemental distribution of Cu and Cr atoms. Majority of the Cu enriched precipitates (with 41 ± 8 at% Cu) are along the columnar grain boundaries.

(caption on next page)

measurements reveal {110}$_{bcc}$ fiber texture (intensity peak maxima at 0° and 60°) as major texture component (see Fig. 10(a)-(f) and Fig. 10(g)). Additional intensity data points at various other tilt angles in Fig. 10(g) indicates the presence of mainly {211} and {210} oriented crystallites. Fig. 10(h) shows the pole widths of {110} Cr poles (pole width is defined as half width at 50% normalized intensity of the peak at or near ψ = 0 from the {110} Cr fiber plots) plotted as a function of annealing temperature. With increasing annealing temperature up to 350 °C, pole width for {110}$_{bcc}$ poles increases (i.e. sharpness of {110}$_{bcc}$ fiber texture of bcc Cr(Cu) phase decreases) and beyond 350 °C, {110}$_{bcc}$ pole width decreases up to 450 °C (i.e. {110}$_{bcc}$ fiber texture sharpens).

Fig. 11(a) and (b) show the measured pole figures corresponding to {111}$_{fcc}$ reflections of fcc Cu(Cr) phase in the 400°C and 450 °C annealed films which reveal {111}$_{fcc}$ fiber texture of Cu(Cr) phase with other close-packed planes of the fcc lattice inclined at 70.5° to each other. Fiber plots corresponding to {111}$_{fcc}$ Cu has been presented in Fig. 11(c). Presence of additional intensity data points at a tilt angle nearly 54.5° indicate the presence of {100} oriented Cu(Cr) crystallites (see Fig. 11(c)). (see Appendix B for the detailed discussion).

3.4. Stress evolution in $Cr_{0.8}Cu_{0.2}$ films

$d_{\psi}^{hkl} - Sin^2\psi$ plots corresponding to {110} and {220} reflections of bcc Cr phase for both as-deposited and annealed $Cr_{0.8}Cu_{0.2}$ films are shown in Fig. 12(a) and (b) respectively. For both as-deposited and annealed films, $d_{\psi}^{hkl} - Sin^2\psi$ plots corresponding to both bcc reflections could be fitted with straight lines with goodness of fit (R^2) exceeding 95% for all data set. A gradual change in slopes of straight lines with increasing annealing temperature implies an increase of tensile strain with increasing annealing temperature (Fig. 12(a) and
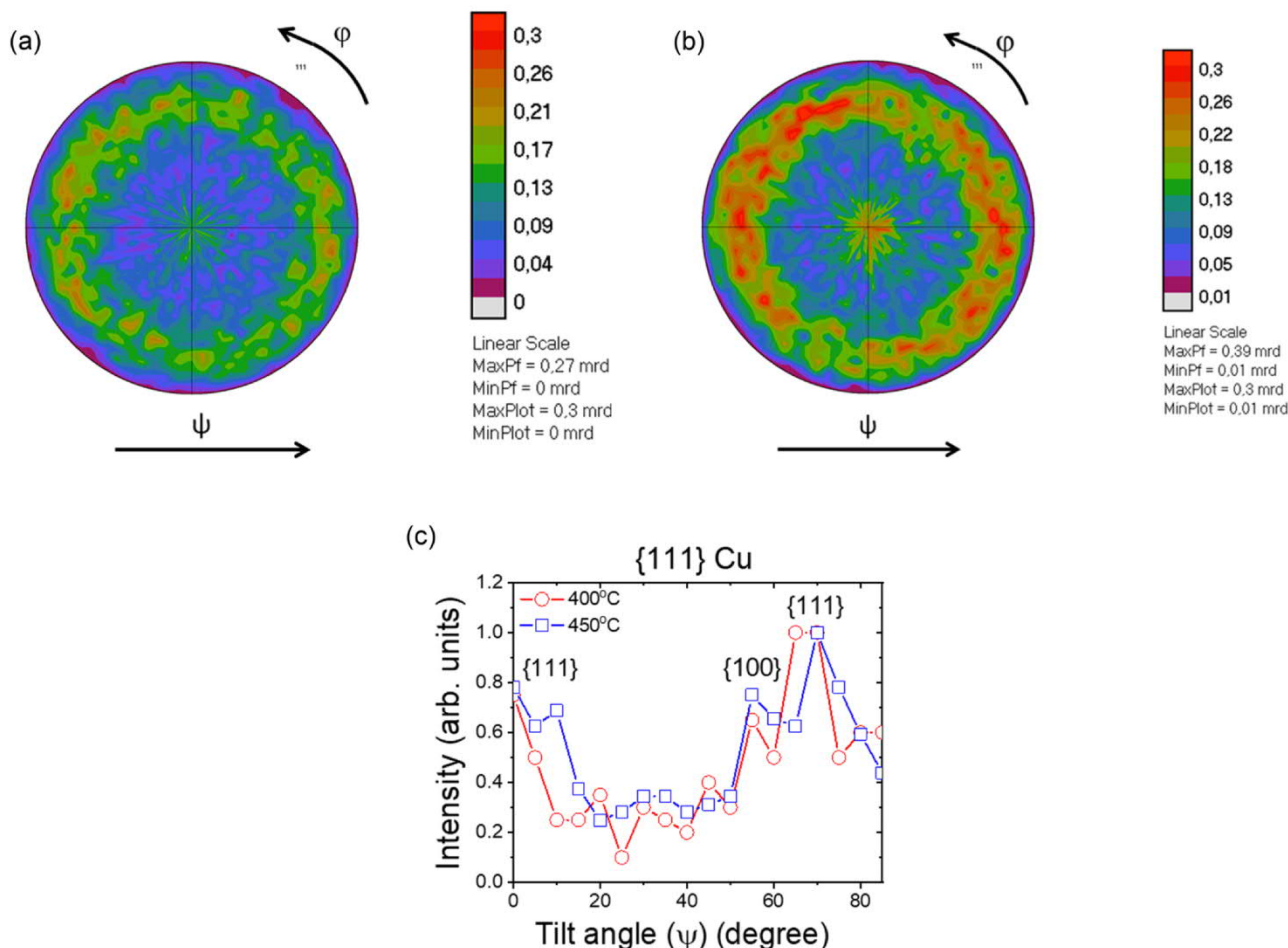
Fig. 12. (a): d-$Sin^2\psi$ plots corresponding to Cr {110} diffraction peak for the as deposited and annealed $Cr_{0.8}Cu_{0.2}$ thin films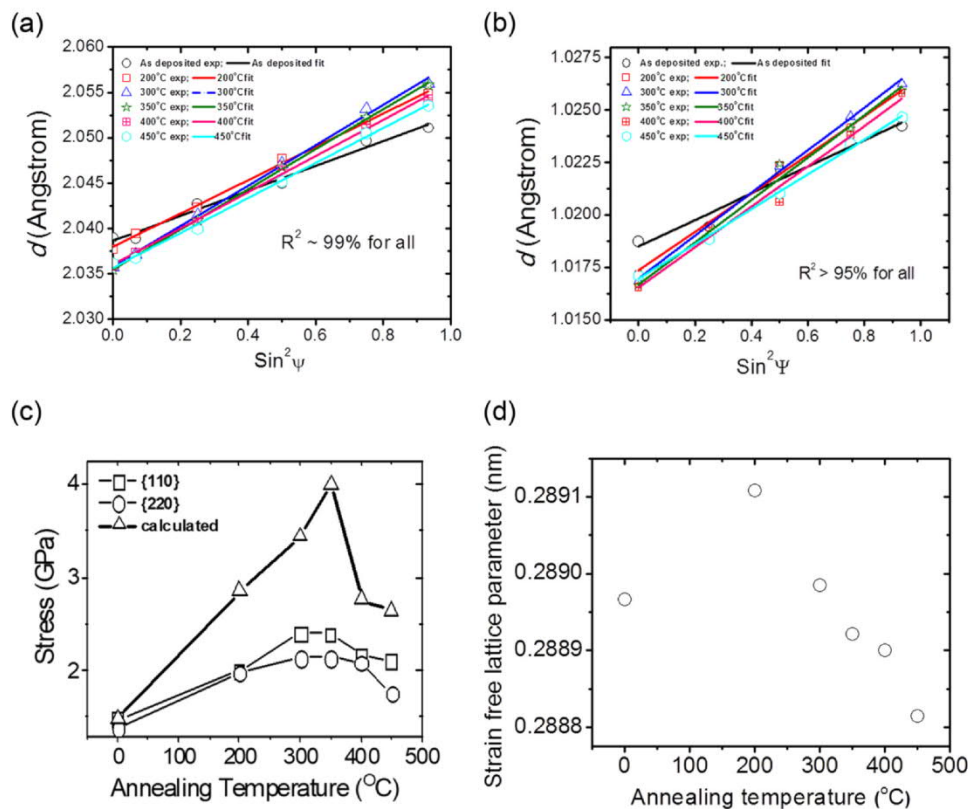. (b): d-$Sin^2\psi$ plots corresponding to Cr {220} diffraction peak for the as deposited and annealed $Cr_{0.8}Cu_{0.2}$ thin films. (c): Tensile stresses in $Cr_{0.8}Cu_{0.2}$ thin films derived from the XRD stress analysis are plotted as a function of annealing temperature. (d): Strain-free lattice parameter of bcc Cr(Cu) phase as a function of annealing temperature.

(b)). Magnitude of tensile stresses (determined from XRD stress analysis) and their variations with annealing temperatures corresponding to both {110} and {220} reflections of bcc Cr phase is shown in Fig. 12(c) along with the theoretically calculated tensile stresses generated due to various microstructural changes occurring in $Cr_{0.8}Cu_{0.2}$ thin films during annealing (see Table-1 & Appendix-B). A general observation is an almost linear increase of biaxial tensile stress in the $Cr_{0.8}Cu_{0.2}$ thin films with increasing annealing temperature at least up to 300 °C beyond which film stress decreases up to 450 °C (Fig. 12(c)). Fig. 12(d) shows strain free lattice parameters of bcc Cr(Cu) phase as a function of the annealing temperature determined from the {110} $d_{\psi}^{hkl} - Sin^2\psi$ plots. In general, a decreasing trend of lattice parameter can be observed below 300 °C except an unexpected increase at 200 °C. At 450 °C, the strain free lattice parameter (0.28881 nm) is very close that of pure bcc Cr phase (bulk value of lattice parameter ~ 0.2884 nm) due to precipitation of the fcc Cu (Cr) phase from the supersaturated bcc solid solution of $Cr_{0.8}Cu_{0.2}$ films. Accurate stress evaluation for the fcc Cu phase was prevented by the strong {111}$_{fcc}$ fiber texture (i.e. insufficient data points in the respective $d_{\psi}^{hkl} - Sin^2\psi$ plots) and overlapping of the {111}$_{fcc}$ reflection with the {110}$_{bcc}$ reflection. (see Appendices B & C for the detailed discussion).

4. Discussion

4.1. Phase stability and microstructure of $Cr_{0.8}Cu_{0.2}$ thin films

The equilibrium phase diagram of Cr-Cu system exhibits almost negligible solid solubility of Cu in bcc Cr (< 0.2 at%) and maximum solubility of 0.8 at% Cr in fcc Cu at 1077 °C [5]. Nevertheless, XRD and APT observations confirmed the formation of $Cr_{0.8}Cu_{0.2}$ alloy having bcc crystal structure in the as deposited thin film even when the substrate temperature did not exceed 102 °C. Such $Cr_{0.8}Cu_{0.2}$ alloy phase is a metastable supersaturated solid solution (since 20 at% Cu in bcc Cr is much larger than equilibrium solubility of Cu in Cr) with higher free energy than the equilibrium. Regular solution type CALPHAD assessment of metastable Cu-Cr system indicates bcc crystal structure of $Cr_{0.8}Cu_{0.2}$ phase with Gibbs free energy of approximately 13KJ/g-atom at 25 °C [6]. Due to inherent metastability the as-deposited $Cr_{0.8}Cu_{0.2}$ alloy thin film will try to reduce its free energy by phase separation during the film deposition and/or during post deposition annealing of the thin film. Phase decomposition in growing co-sputtered $Cu_{0.9}Cr_{0.1}$ thin films has been observed by McIntyre et al. at substrate temperature ~105 °C [3]. In contrast, Kim and Yee did not find any sign of phase decomposition in the $Cr_{0.5}Cu_{0.5}$ thin film during deposition up to substrate temperature of ~275 °C [11]. To this end, Harzer et al. have further suggested that the single phase bcc metastable Cr-Cu thin films with higher Cr composition should exhibit higher stability [10]. From a kinetic viewpoint, the as deposited $Cr_{0.8}Cu_{0.2}$ thin film should be stable during the film deposition since the mobilities of the condensed atomic species are essentially restricted even at the maximum substrate temperature of 102 °C (for 100 min of film deposition at 102 °C substrate temperature, the theoretically estimated diffusion distances (~2 $\sqrt{Dt}$ where D is the diffusion coefficient) are 10^{-6} nm for Cu diffusion in bcc Cr (diffusion coefficient ~2 × 10^{-34} m²/s) and 10^{-5} nm for Cr diffusion in fcc Cu (diffusion coefficient ~2 × 10^{-32} m²/s) [69–71]). However, a detailed APT investigation of as-deposited thin films revealed fine precipitates (diameter ~3 nm) having 31.5 at% Cu (or 68.5 at% Cr) in the Cr rich bcc Cr(Cu) matrix with global composition of $Cr_{0.8}Cu_{0.2}$ (Fig. 7(a)). Such APT observation indicates local compositional fluctuation within the virtually homogeneous single phase $Cr_{0.8}Cu_{0.2}$ solid solution and this seems to be the onset of phase separation in the as-deposited alloy thin film. Since the

conventional Bragg diffraction is not sensitive to such local (or short range) compositional inhomogeneity or phase decomposition at a very fine length scale (a few nm or so), X-ray diffraction of as-deposited thin film showed single Bragg pattern corresponding to bcc $Cr_{0.8}Cu_{0.2}$ phase instead of individual Bragg patterns corresponding to locally varying lattice parameters. Thermodynamic assessment of metastable equilibrium in Cr-Cu binary system indicates that the $Cr_{0.8}Cu_{0.2}$ alloy composition lies well within the spinodal region of the miscibility gap in the Cr-Cu phase diagram for the temperature range of interest (~25°C to 450°C) [54]. Hence, the as deposited $Cr_{0.8}Cu_{0.2}$ thin film may undergo phase separation via spinodal decomposition regime where it can reduce its free energy by such compositional fluctuation if it is periodic and having large spatial extent within the solid solution [72,73].

During annealing of $Cr_{0.8}Cu_{0.2}$ thin films, the existing compositional fluctuations/clusters with Cu composition ~ 31.5 at% in the bcc Cr(Cu) matrix may spontaneously change their Cu composition due to up-hill diffusion of Cu and Cr atoms between the matrix and the clusters. The kinetics of this process strongly depends on the temperature dependent atomic mobilities of Cu and Cr (i.e. their diffusion coefficients). However, the available inter-diffusion data in binary Cr-Cu alloys suggests that the bulk (lattice) diffusion coefficient of Cu in bcc Cr (~ 2.75×10^{-21} m^{2}s^{-1}) is more than two orders of magnitude smaller than that of Cr in fcc Cu (~ 1.5×10^{-19} m^{2}s^{-1}) even at the highest annealing temperature (~450°C) [69,70]. Therefore, Cu composition change in the clusters takes more time (due to slow rejection of Cu atoms from the matrix) compared to the migration of Cr atoms and the formation of Cr rich bcc matrix. Thus, kinetically, the formation of pure fcc Cu (i.e. close to 100% Cu) precipitate phase is hindered especially at relatively low temperature of annealing (~ at 300°C). Thermodynamically, nucleation of pure fcc Cu precipitate is also not favored mainly because of high interface energy (~ 0.72 J/m^2) especially if the matrix-precipitate interface is incoherent (see Appendix A.1 for details). On the other hand, bcc Cr(Cu) matrix also cannot be 100% Cr rich due to the slow kinetics of the process at 300°C and hence the formation of an intermediate precipitate phase having Cr composition less than the bcc $Cr_{0.8}Cu_{0.2}$ matrix may be favored when the Cu content in the clusters reaches a critical value. XRD evidence of such composition modulation and possible growth of 'less Cr rich' intermediate precipitate composition has been confirmed for the film annealed at 300°C for 45 min (see Fig. 3(a) for arrow marked diffraction signal which is the 'side band' (satellite) reflection on the left side of the {110} Cr diffraction peak corresponding to mean composition of the film). Appearance of such side band reflection is a typical signature of phase separation of $Cr_{0.8}Cu_{0.2}$ solid solution by spinodal decomposition during isothermal annealing of the thin film. However, the right hand side satellite reflection is too weak to be unambiguously detected perhaps due to imperfect composition modulation. APT observation of 300°C, 2.5 h annealed thin film confirmed presence of such intermediate precipitates with Cu composition ~ 43.2 at% (i.e. 56.8 at% Cr) both inside the grains and at the GB adjacent regions in the Cr(Cu) matrix (see Section 3.2; Fig. 8(a) and (b)). Gibbs free energy curve of metastable Cr-Cu system suggests bcc crystal structure of such intermediate precipitates with approximate chemical composition of $Cr_{0.6}Cu_{0.4}$ [6] (note: nucleation of metastable fcc $Cr_{0.6}Cu_{0.4}$ phase is not possible, see Appendix A.2). The intragranular bcc $Cr_{0.6}Cu_{0.4}$ precipitates must be coherent with the bcc Cr(Cu) matrix in order to minimize the coherency strain energy during the spinodal decomposition which must proceed continuously throughout the matrix (see Appendix A.3 for thermodynamic calculation of precipitate-matrix interface energy (~0.038 J/m^2)). Additionally, precipitates adjacent to the GBs possibly suggests the role of Cu diffusion through the columnar GBs of the bcc Cr(Cu) matrix combined with limited sideways bulk (lattice) diffusion of Cu inside the film matrix (GB diffusion coefficient of Cu in bcc Cr > > corresponding bulk (lattice) diffusion

coefficient at 300°C) [69,70]. In this context, it must be noted that majority of the research works on both bulk and thin films of Cr-Cu alloys reported reasonably good thermal stability up to 300°C annealing temperature [11–14,68,74]. Precipitation of similar metastable phases is known to occur in number of alloy systems particularly in age hardened Al based alloys [75–77]. Nevertheless, such intermediate bcc $Cr_{0.6}Cu_{0.4}$ precipitates are thermodynamically metastable and at higher annealing temperature (~ 350°C), preferably the GB adjacent precipitates may undergo Cu composition change by faster GB diffusion of Cu atoms (see circle marked diffraction peak in Fig. 3(b)). However, the intra-granular metastable precipitates cannot change their Cu composition appreciably due to limited bulk diffusion distance of Cu atoms in bcc Cr (~ 0.4 nm for 45 min annealing at 350°C) (see arrow marked reflection from such precipitates in Fig. 3(b)). Beyond 350°C annealing temperature, negligible growth of bcc Cr(Cu) crystallites (see Fig. 6(a)) is possibly due to the precipitation of Cu(Cr) phase at the GB adjacent regions due to so called grain boundary pinning [78].

Longer duration of annealing (≥45 min) at temperature ≥400°C leads to formation of significant volume fraction of Cu rich stable fcc Cu(Cr) phase with lattice parameter close to that of pure Cu (see Fig. 5 and large integrated intensities of prominent {111}Cu diffraction peaks in Fig. 3(c) and (d)). Growth kinetics of such fcc Cu(Cr) precipitates seems to involve two different regimes as pointed out earlier from a qualitative analysis of the time evolution of volume fraction of the fcc Cu(Cr) phase (see XRD results and interpretation from Fig. 5 in Section 3.1). During the early stage of annealing at 450°C (~ up to 30 min) phase separation may proceed through spinodal decomposition regime where the intermediate metastable bcc $Cu_{0.4}Cr_{0.6}$ precipitates form and grow throughout the film matrix (see arrow marked reflection in Fig. 4(b)). Besides, a small volume fraction of Cu rich stable fcc Cu(Cr) precipitates form due to change of Cu composition preferably in the GB adjacent metastable precipitates by predominant GB diffusion of Cu atoms and sideways limited bulk diffusion (see Fig. 5 and the {111} Cu diffraction peak in Fig. 4(b) and (c)). Growth kinetics of such GB adjacent stable fcc Cu (Cr) precipitates does not follow JMAK empirical equation [67] for annealing duration ≤ 30 min as indicated earlier (see Section 3.1). Additionally, a strong overlapping between {111} Cu diffraction peak from the fcc Cu phase and the arrow marked diffraction signal from the metastable bcc precipitates (see Fig. 4(c)) suggests gradual change of Cu composition even within the intra-granular precipitates despite sluggish bulk diffusion process (diffusion distance of Cu atoms in bcc Cr ~ 4 nm). In fact, evidence of similar Cu composition increase in the metastable precipitates is found even for 45 min annealing at 350°C (see Fig. 3(b)) where the bulk diffusion distance of Cu atoms in bcc Cr < 1 nm. Such observation suggests that, possibly, the metastable bcc precipitates randomly distributed both inside the columnar grains and at the GB adjacent regions have acted as heterogeneous nucleation sites in order to initiate faster nucleation and growth of the stable fcc Cu(Cr) precipitates with lattice parameter close to that of pure Cu during the subsequent stage of annealing. In this context, it is to note that numerous GBs in the bcc Cr(Cu) matrix could be the heterogeneous nucleation sites as well for direct nucleation of pure fcc Cu precipitates. Theoretically estimated nucleation barrier for the heterogeneous nucleation of fcc Cu(Cr) phase on the bcc $Cu_{0.4}Cr_{0.6}$ precipitate (~ 5.8×10^{-20} J) is of the same order of magnitude as the heterogeneous nucleation barrier estimated for the nucleation of fcc Cu(Cr) precipitates at the columnar GBs (~ 5.2×10^{-20} J) and therefore both the phenomena may come into strong competition with each other (see Section 4.2 and Appendix A.5). However, thermodynamic calculation further suggests that the presence of such metastable bcc $Cu_{0.4}Cr_{0.6}$ precipitates both inside the grains and at the columnar GBs of the bcc Cr(Cu) matrix is favored as compared to the fcc Cu phase (see Appendix A.5). Therefore, it is plausible that fcc Cu(Cr) phase nucleates on the

metastable bcc $Cu_{0.4}Cr_{0.6}$ precipitates as the later phase form during the very early stage of phase decomposition. Such heterogeneous nucleation of fcc phase is known to occur in Al-Cu alloys [71,79].

For longer annealing duration (> 30 min and up to 1 h) at 450°C, the heterogeneous nucleation and growth of stable fcc Cu(Cr) precipitates continues by simultaneous GB diffusion and bulk diffusion of Cu atoms from the matrix to the precipitates which leads to almost complete disappearance of the bcc metastable precipitates and finally the formation of a two-phase structure (i.e. stable fcc Cu(Cr) phase + bcc Cr(Cu) matrix) (see Fig. 5 and Fig. 4(d)). Growth kinetics of such stable fcc Cu(Cr) precipitates for annealing duration > 30 min follows the JMAK empirical law [67] as revealed earlier (see Fig. 5 and Section 3.1). It is further important to note that the JMAK empirical law is not applicable in case of heterogeneous nucleation at special sites such as periodically spaced columnar GBs in the film matrix [67]. The heterogeneous nucleation of fcc Cu(Cr) phase on the dislocations has not been considered in this work. TEM observation of Cu enriched regions (average size ~ 14 ± 4 nm) along the columnar GBs in the 450°C, 1 h annealed thin film indicates precipitate coarsening at the GB regions. Observation of {111} Cu reflections in the SAD pattern confirms fcc Cu(Cr) phase in such annealed film (see Fig. 9(b)). However, STEM-EDS measurement of 41 ± 8 at% Cu seems to underestimate the Cu composition in such precipitates which may be due to the fact that the EDS measurements is always influenced by the contribution of the matrix (the matrix is less Cu rich as compared to fcc Cu precipitate). Therefore, just to summarize, the kinetics of phase decomposition of supersaturated $Cr_{0.8}Cu_{0.2}$ thin film during isothermal annealing starts with spinodal type of decomposition process via metastable bcc intermediate phase formation and ends with nucleation and growth of Cu rich stable fcc Cu(Cr) precipitate phase for longer duration of annealing at higher temperature. Phase decomposition studies of several supersaturated Cu-Cr alloys by differential scanning calorimetry (DSC) exhibit two or more overlapping very broad DSC peaks which indicates that the kinetics of phase decomposition over the entire annealing temperature range cannot be understood by a single and simple mechanism (i.e. decomposition process is always a mixture of spinodal decomposition and nucleation and growth processes) [6,7,23,80].

4.2. Phase separation in $Cr_{0.8}Cu_{0.2}$ thin films: thermodynamic considerations

Experimental results discussed in the previous section demonstrate that the phase decomposition of metastable nanocrystalline $Cr_{0.8}Cu_{0.2}$ thin film involves formation of metastable bcc $Cr_{0.6}Cu_{0.4}$ precipitate phase during the early stage of phase separation. However, such intermediate precipitate phase contains significant amount of Cr (~ 60 at%) which is quite unexpected because of the very limited solid solubility between Cu and Cr at 300°C and 450°C. From the Cu-Cr equilibrium phase diagram, at 450°C, theoretically calculated solid solubility of bcc Cr in fcc Cu is 0.0125 at% and the solubility of fcc Cu in bcc Cr is 0.00014 at% [5]. This means that equilibrium thermodynamics only predicts precipitation of pure Cu phase (~ 99.9% Cu) following classical nucleation theory. Kinetic arguments considered earlier predicted that formation of such metastable precipitate phase involves spinodal type of decomposition mechanism. In the following, thermodynamic considerations will be explored in order to understand the non-classical nucleation of such metastable $Cr_{0.6}Cu_{0.4}$ phase and finally the nucleation of Cu rich stable fcc Cu(Cr) phase with lattice parameter close to Cu. At first, classical nucleation barrier for pure fcc Cu precipitates has been estimated by calculating the chemical driving force (Δg_n), elastic strain energy density (Δg_{el}) and interfacial energy (γ) which come into competition during classical nucleation [44,81,82] (see

Appendix A.1 for detailed formalism and calculation). Applying regular solution model [44,83,84] to Cu-Cr binary alloy system, the magnitude of classical nucleation barrier for a pure fcc Cu nucleus $((\Delta f^*)_{homo-classical-fccCu})$ has been calculated as ~ 6×10^{-20} J for thin film annealed at 450°C. This value of classical nucleation barrier will be compared to those calculated for the intermediate precipitate phase having 40 at% Cu (i.e. $Cr_{0.6}Cu_{0.4}$) observed experimentally. At first, it will be assumed that $Cr_{0.6}Cu_{0.4}$ precipitates have fcc crystal structure. Nucleation barrier fcc $Cr_{0.6}Cu_{0.4}$ phase has been calculated using the so called 'non-classical nucleation' theory [44,85–89] (see Appendix A.2 for detailed formalism and calculation). For the thin film annealed at 450°C, the non-classical nucleation barrier of fcc $Cr_{0.6}Cu_{0.4}$ precipitate $(\Delta f^*_{homo-non-classical-fcc\ Cr0.6Cu0.4})$ has been calculated as ~ 3×10^{-17} J which is nearly three orders of magnitude higher than the classical nucleation of pure fcc Cu phase. Therefore, the homogeneous nucleation of fcc $Cr_{0.6}Cu_{0.4}$ precipitate is questionable. To this end, it may be noted that the higher nucleation barrier in case of nucleation of fcc $Cr_{0.6}Cu_{0.4}$ precipitate is due to high value of the precipitate-matrix interface energy which is assumed to be incoherent as precipitate and matrix have different crystal structures. The critical radius ($r^* = 2\gamma/(\Delta g_n + g_{el-misfit})$) of fcc $Cr_{0.6}Cu_{0.4}$ nucleus is 3 nm which is however a realistic value in the early stage of precipitation. Therefore, it is easier to nucleate pure fcc Cu precipitate having nearly 100 at% Cu compared to those having 40 at% Cu composition. However, experimental observations indicate presence of bcc $Cr_{0.6}Cu_{0.4}$ precipitates which will be considered in the following.

The nucleation barrier for bcc $Cr_{0.6}Cu_{0.4}$ precipitate has been calculated using non-classical nucleation theory and compared with those obtained for the pure fcc Cu and fcc $Cr_{0.6}Cu_{0.4}$ precipitates. Such bcc $Cr_{0.6}Cu_{0.4}$ precipitates phases are assumed to be coherent with the bcc Cr(Cu) matrix as the precipitate and matrix have identical crystal structure. The nucleation barrier height of the bcc $Cr_{0.6}Cu_{0.4}$ precipitate $(\Delta f^*_{homo-nonclassical-bcc\ Cr0.6Cu0.4})$ has been calculated as 4.5×10^{-21}J (see Appendix A.3 for details) which is four orders of magnitude smaller than that of the fcc $Cr_{0.6}Cu_{0.4}$ precipitates and one order of magnitude smaller than that of the pure fcc Cu precipitate. Therefore, it seems that nucleation of bcc $Cr_{0.6}Cu_{0.4}$ precipitates is much easier than both pure fcc Cu precipitate and metastable fcc $Cr_{0.6}Cu_{0.4}$ precipitate. In this context, it may be noted that transmission electron diffraction did not reveal a fcc phase for the $Cr_{0.6}Cu_{0.4}$ precipitates supporting the statement of a bcc crystal structure. However, subtle fcc reflections could be too weak to be recorded. Furthermore, XRD and APT evidences combined with CALPHAD calculation confirm formation of metastable $Cr_{0.6}Cu_{0.4}$ precipitates having bcc crystal structure (see Section 4.1).

Finally, for a complete understanding of the early stage of phase separation, nucleation of pure bcc Cu precipitates (~ 99.9% Cu) assumed to be coherent with the bcc Cr(Cu) matrix has been considered employing the classical nucleation theory (see Appendix A.4 for details). The nucleation barrier height for coherent bcc Cu precipitates $((\Delta f^*)_{homo-classical-bcc\ Cu})$ has been calculated as 1.5×10^{-21}J which is the smallest nucleation barrier compared to those calculated for all other precipitates considered above. The elastic strain energy density of bcc Cu precipitates coherent with the bcc Cr(Cu) matrix is negligible because of the negligible misfit between the precipitate and the matrix. This suggests that the nucleation of pure bcc Cu phase is the easiest as compared to all other precipitate phases. However, neither TEM nor XRD has detected unambiguous presence of such bcc Cu phase due to very close lattice parameters of bcc Cr(Cu) matrix (i.e. 0.28881 nm) and bcc Cu phase (i.e. 0.287 nm) [90]. Furthermore, formation of bcc Cu nuclei via classical nucleation theory is very much unlikely during the early stage of phase separation since already APT investigation of the

as-deposited $Cr_{0.8}Cu_{0.2}$ thin film revealed presence of fine precipitates (~ 3 nm diameter) with 31.5 at% Cu in the bcc Cr(Cu) matrix which is the onset of phase separation in the film via spinodal decomposition.

Therefore, the above thermodynamic calculation indicates that the early stage of precipitation in the annealed $Cr_{0.8}Cu_{0.2}$ film started with the localized formation of bcc $Cr_{0.6}Cu_{0.4}$ phase (nucleation barrier ~ 4.5×10^{-21}J) which is coherent with the bcc Cr (Cu) matrix with the lowest interface energy ($\gamma_{coherent-bcc\ Cr0.6Cu0.4}$~0.038J/m^2) among all phases considered above. Furthermore, the nucleation barrier of heterogeneous nucleation of such bcc $Cr_{0.6}Cu_{0.4}$ precipitates at the columnar GBs has been theoretically estimated as 1.3×10^{-21}J which is one order of magnitude smaller than the nucleation barrier for the direct heterogeneous nucleation of fcc Cu phase at the GBs (5.2×10^{-20}J) (see Appendix A.5). Therefore, theoretically, metastable bcc $Cr_{0.6}Cu_{0.4}$ precipitates can be present both at the columnar GBs and inside the grains in bcc Cr(Cu) matrix. Since such bcc $Cr_{0.6}Cu_{0.4}$ precipitate phase is thermodynamically metastable in nature, as they grow in size their stability decreases for longer duration of annealing at temperature ≥ 350°C and they get gradually transformed into Cu rich stable fcc Cu(Cr) phase by continuous diffusion of Cu atoms from the Cr(Cu) matrix. Since bulk diffusion process is sluggish (diffusion distance of Cu atoms in bcc Cr < 1 nm), it is proposed that at temperature ≥ 350°C, metastable $Cr_{0.6}Cu_{0.4}$ phases formed during the early stage of annealing both inside the grains and at the GB adjacent regions may act as heterogeneous nucleation sites for the nucleation and growth of the stable Cu rich fcc Cu(Cr) phase at higher annealing temperature.

5. Conclusions

The present work investigates phase separation mechanism of MBE grown nanometer thick $Cr_{0.8}Cu_{0.2}$ thin alloy films by XRD, APT and high resolution TEM combined with EDS. In addition, evolution of microstructure, stress development and texture evolution have been studied. Following are the major conclusions:

1. XRD investigation of the as deposited thin films confirms formation of $Cr_{0.8}Cu_{0.2}$ phase having bcc crystal structure whereas APT investigation has revealed presence of fine precipitates in the bcc Cr(Cu) matrix which suggests the onset of phase separation already in the as-deposited thin film by spinodal type of decomposition.
2. Kinetics of phase decomposition during annealing of the thin films seems to be a two-step process: (i) during the early stage of annealing (~300°C), phase decomposition may proceed via spinodal decomposition regime which leads to the formation of intermediate bcc metastable phase (~ $Cr_{0.6}Cu_{0.4}$) observed both inside the grains and at the GB adjacent regions of the bcc Cr(Cu) matrix; (ii) upon continued annealing at 350°C for more than 45 min, such metastable $Cr_{0.6}Cu_{0.4}$ precipitates could act as heterogeneous nucleation sites for the observed onset of precipitation of Cu rich fcc Cu(Cr) phase. Annealing at temperature ≥ 400°C for longer duration (≥ 45 min) leads to the formation of a

two phase structure (fcc Cu(Cr) phase + bcc Cr(Cu) matrix) which crystallographically completes the phase separation of nanocrystalline $Cr_{0.8}Cu_{0.2}$ thin films while the compositions have not yet reached thermodynamic equilibrium.
3. Annealing of the thin films at temperature ≥ 350°C has led to the relaxation of microstrain due to annihilation of lattice defects. Tensile growth stresses (~1.5 GPa) in the as-grown thin film has got relaxed after annealing the film above 350°C predominantly due to the compressive stress generation from the Cu(Cr) precipitation at the grain boundaries of Cr(Cu) matrix. Additionally, such stress relaxation is accompanied by an increase of strength and sharpness of {110} fiber texture of bcc Cr(Cu) matrix phase. Relaxation of macrostresses and microstrains minimizes the total strain energies of the thin films and observed crystallographic textures reduce the films surface energies. This leads to a net reduction of the total Gibbs free energy of the films which is one of the major thermodynamic driving forces for the observed phase decomposition of the $Cr_{0.8}Cu_{0.2}$ thin films.
4. Thermodynamic model calculation indicates possibility of non-classical nucleation of such metastable bcc $Cr_{0.6}Cu_{0.4}$ precipitates in the bcc Cr(Cu) matrix. Such precipitates, coherent with the bcc Cr (Cu) matrix have the lowest minimum interface energy. Theoretical calculation further suggests that such metastable bcc precipitates can be present both inside the grains and at the columnar GBs in the bcc Cr(Cu) matrix which may act as heterogeneous nucleation sites for the subsequent nucleation and growth of Cu rich stable fcc Cu(Cr) phase for longer duration annealing at temperature ≥ 350°C.

CRediT authorship contribution statement

J. Chakraborty: XRD data curation and analysis, thermodynamic analysis, Writing – original draft. **T. P. Harzer:** Film deposition and annealing, TEM data curation and analysis. **Jazmin Duarte:** APT data curation and analysis. **Gerhard Dehm:** Funding acquisition, Conceptualization and guidance.

Declaration of Competing Interest

The authors declare that they have no known competing financial interests or personal relationships that could have appeared to influence the work reported in this paper.

Acknowledgements

Appendix A1. Calculation of classical nucleation barrier for pure fcc Cu precipitates

Classical nucleation barrier for pure fcc Cu precipitates has been estimated by calculating the chemical driving force, elastic strain energy density and interfacial energy. Applying regular solid solution model to Cu-Cr binary alloy system the driving force for classical nucleation (Δg_n, the chemical driving force from the chemical Gibbs free energy change upon nucleation) in dilute alloys can be written as [44,81,82]:

$$(\Delta g_n)_{Classical} = \left(\frac{RT}{V_\beta}\right) X_\beta \ln\left(\frac{X_o}{X_\alpha}\right) \tag{A1}$$

where X_β is the Cu concentration (expressed in atom fraction) in the Cu(Cr) precipitates, X_o is the atom fraction of Cu solute dissolved in Cr-Cu homogeneous solid solution in the as deposited thin films. X_α is the equilibrium solubility of fcc Cu in bcc Cr phase. X_α has been calculated as

1.4×10^{-4} at 450°C from the available thermodynamic data corresponding to equilibrium Cu-Cr phase diagram [5]. V_β, the molar volume of fcc Cu phase is taken as 7.12×10^{-6} m³/mole. For pure fcc Cu precipitate (100 at% Cu in classical nucleation theory), $X_\beta \sim 1$ since $X_\alpha < < 1$. The calculation has been done for $X_o = 0.2$. Putting the above values, $(\Delta g_n)_{Classical-fcc\,Cu} = 1 \times 10^{10}$J/m³ for the nucleation of pure fcc Cu precipitates has been obtained. In the following, the above chemical driving force will be compared to elastic strain energy originating mainly from misfit stress between fcc Cu precipitate-bcc Cr(Cu) matrix and the energy of the precipitate-matrix interface. In this case, the precipitate and the matrix have different crystal structures and the interface is assumed to be incoherent. Elastic strain energy density $(\Delta g_{el-misfit-incoherent})(=(\sigma_{misfit})^2/M_{Cr(Cu)})$ due to misfit can be expressed as follows [36]:

$$\Delta g_{el-misfit-incoherent} = M_{Cr(Cu)} \times \frac{1}{9} \times \left| \frac{V_{fccCu(Cr)} - V_{bccCr(Cu)}}{V_{bccCr(Cu)}} \right|^2 \tag{A2}$$

Where $V_{bccCr(Cu)}$ and $V_{fccCu(Cr)}$ are the specific volumes (volume/atom) of the bcc Cr(Cu) phase and the fcc Cu(Cr) precipitate phase respectively. $M_{Cr(Cu)}$ is the biaxial modulus of {111}fiber textured Cr phase (~ 333 GPa) [95]. For the bcc Cr(Cu) matrix phases, specific volumes have been calculated from the corresponding strain free lattice parameters at different annealing temperatures (shown in Fig. 12(d)). For fcc Cu (Cr) precipitates, a constant specific volume of 11.9 (Å)³/atom (calculated from the lattice parameter corresponding to 450°C) has been used since precise lattice parameter determination of fcc Cu(Cr) phase has not been possible at other annealing temperatures due to broadened and weak {111} fcc Cu(Cr) peak overlapped with {110} Cr(Cu) peak in the XRD pattern. The calculated elastic strain energy density resulting from the misfit at 450°C annealing temperature is $\Delta g_{el-misfit-incoherent} = 5.6 \times 10^6$J/m³ which is four orders of magnitude smaller than the chemical driving force for classical nucleation. Fig. 13 shows the plot of total elastic strain energy density (Δg_{el}) of the bcc Cr(Cu) matrix (calculated from the experimentally determined stress values presented in Fig. 12(c) in the Cr(Cu) matrix) with various annealing temperatures.
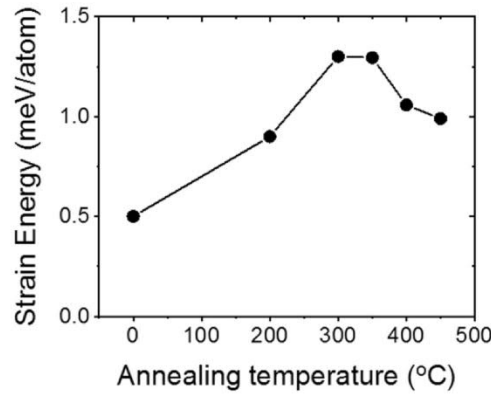

Fig. 13. Strain energy (Δg_{el}; meV/atom) of bcc Cr(Cu) matrix at various annealing temperatures.

Next consideration is the energy of the interface between the pure fcc Cu precipitate (assuming 100% Cu content in the fcc Cu(Cr) precipitate) and the bcc Cr matrix (assumed 100% Cr in the Cr(Cu) matrix). The precipitate and the matrix have different crystal structures and the interface is assumed to be incoherent. Energy of such incoherent interface (γ_{Cu-Cr}) can be estimated using the following equation [91]:

$$\gamma_{Cu-Cr} = \frac{1}{3} \left(\frac{\gamma_{Cu} + \gamma_{Cr}}{2} \right) + \frac{\Delta H_{Cr\,in\,cu}^{interface}}{C_o V_{Cr}^{2/3}} \tag{A3}$$

where, the first term in Eq. (A3) is related to the strain due to the mismatch at the interface between two lattices (fcc Cu and bcc Cr) and the second term is related to the chemical interaction of fcc Cu precipitate and bcc Cr matrix at the interface. and γ_{Cr} are the surface energies of pure Cu and pure Cr respectively. $\Delta H_{Cr\,in\,cu}^{interface}$ is the enthalpy increase per mole of Cu atoms at the interface. V_{Cr} is the molar volume of bcc Cr phase (~ 7.23×10^{-6} m³/mole). C_o is a constant depending on the shape of the Wigner-Seitz cell of Cu atoms and can be taken on average as 4.5×10^8 [91]. By putting the values of and γ_{Cr} as 1825 mJ/m² and 2300 mJ/m² respectively and $\Delta H_{Cr\,in\,cu}^{interface}$ as 51 kJ/mole [91], the interface energy is calculated as 0.717 J/m² which is a typical value for the energy of an incoherent interface between two different phases having different crystal structures. Thus nucleation barrier for homogeneous nucleation of pure fcc Cu precipitates (Δf_{hom}^*) can be calculated using Eq. (A4) as follows [67,83,84].

$$\Delta f_{hom}^* = \frac{16\pi}{3} \frac{\gamma^3}{(\Delta g_n + \Delta g_{el-misfit})^2} \tag{A4}$$

where γ is the interface energy. Therefore, putting $\gamma = \gamma_{Cu-Cr} = 0.717$ J/m², $(\Delta g_n)_{Classical-fccCu} = 1 \times 10^{10}$J/m³ and $\Delta g_{el-misfit-incoherent} = 5.6 \times 10^6$J/m³ in Eq. (A4), the magnitude of classical nucleation barrier for an fcc Cu nucleus can be calculated as $(\Delta f^*)_{homo-classical-fccCu} \sim 6 \times 10^{-20}$J. The radius of the critical nucleus (r^*) predicted by classical nucleation theory ($r^* = 2\gamma/(\Delta g_n + \Delta g_{el-misfit})$) is 1.4×10^{-10}m which is smaller than the atomic diameter and therefore seems to be unrealistic.

Appendix A.2. Calculation of non-classical nucleation barrier for the metastable fcc $Cr_{0.6}Cu_{0.4}$ precipitates

According to the non-classical nucleation theory [85–89, 44], the driving force for nucleation of precipitates having solute content X_β can be written as:

$$(\Delta g_n)_{non-classical} = \left(\frac{RT}{V_\beta}\right)\left[\frac{2}{\eta}(X_\beta - X_o)^2 - \left(X_\beta \ln\left(\frac{X_\beta}{X_o}\right) + (1 - X_\beta)\ln\left(\frac{1 - X_\beta}{1 - X_o}\right)\right)\right] \tag{A5}$$

where $\eta = T/T_c$ and $T_c = Z\varepsilon/2k$ with ε being the ordering effective energy ($\varepsilon = \Omega/NZ$ where Ω = interaction parameter, N = Avogadro number and Z(coordination number) = 12 for fcc and 8 for bcc) and k = Boltzmann constant. For fcc $Cr_{0.6}Cu_{0.4}$ precipitates, ε has been calculated as 1.6×10^{-20}J where $\Omega_{fcc} = 1.15 \times 10^5$J/mole at $T = 450^\circ$C. $T_c = 6956$ K at $T = 450^\circ$C and thus $\eta = 0.1$. Molar volume of fcc $Cr_{0.6}Cu_{0.4}$ phase has been calculated as $V_{Cr0.6\ Cu0.4} \sim 7.18 \times 10^{-6}$m³/mole. Taking Cu concentration $X_\beta = 0.41$ from the EDS measurement for the 450°C annealed films, the chemical driving force for non-classical nucleation of fcc $Cr_{0.6}\ Cu_{0.4}$ precipitates becomes $(\Delta g_n)_{non-classical-fccCr0.6Cu0.4} = 0.58 \times 10^9$J/m³ which is more than one order of magnitude smaller than the chemical driving force obtained for pure fcc Cu precipitates from the classical nucleation theory. Furthermore, for non-classical nucleation of fcc $Cr_{0.6}Cu_{0.4}$ precipitate, elastic misfit strain energy will be less than 5.6×10^6J/m³ (see above) due to lower Cu content in the fcc $Cr_{0.6}\ Cu_{0.4}$ precipitate (lower than pure fcc Cu precipitate) and thereby lower volume misfit with the Cr(Cu) matrix having global composition $Cr_{0.8}Cu_{0.2}$. Therefore, in this case, elastic strain energy will be more than three orders of magnitude smaller than the chemical driving force $((\Delta g_n)_{non-classical-fccCr0.6Cu0.4})$. On the other hand, the energy of the interface between the fcc precipitates with composition $Cr_{0.6}Cu_{0.4}$ and the bcc Cr(Cu) matrix (assuming 100%Cr composition) can be significant especially if the interface is incoherent and this can be calculated as follows using the following equation [91]:

$$\gamma_{Cr(Cu)-\ fcc\ Cr_{0.6}Cu_{0.4}} = \frac{1}{3}\left(\frac{\gamma_{Cr_{0.6}Cu_{0.4}}\ +\ \gamma_{Cr}}{2}\right) + \frac{F_{Cu}^{Cr}}{C_o}\frac{\Delta H_{Cr\ in\ cu}^{interface}}{V_{Cr}^{2/3}} \tag{A6}$$

$\gamma_{Cr_{0.6}Cu_{0.4}}$ and γ_{Cr} are the surface energies of $\gamma_{Cr_{0.6}Cu_{0.4}}$ phase and pure Cr phase respectively. F_{Cu}^{Cr} is the degree to which Cr atoms are surrounded by Cu atoms and it is given by the following equation [91]:

$$F_{Cu}^{Cr} = C_{Cu}^s = \frac{(1 - 0.6)V_{Cu}^{2/3}}{0.6V_{Cr}^{2/3} + 0.4V_{Cu}^{2/3}} \tag{A7}$$

and

$$\gamma_{Cr_{0.6}Cu_{0.4}} = C_{Cr}^s\gamma_{Cr} + C_{Cu}^s\gamma_{Cu} - C_{Cr}^s C_{Cu}^s\frac{\Delta H_{Cr\ in\ cu}^{interface}}{C_o V_{Cr}^{2/3}} \tag{A8}$$

The surface energy of fcc $Cr_{0.6}Cu_{0.4}$ has been calculated as 2 J/m² and the interface energy $\gamma_{Cr(Cu)-Cr_{0.6}Cu_{0.4}}$ has been calculated as 0.84 J/m² using the numerical values for all the parameters described in Eqs. (A6–A8). The corresponding non-classical nucleation barrier of fcc $Cr_{0.6}Cu_{0.4}$ precipitate has been calculated as $\Delta f^*_{homo-non-classical-fcc\ Cr0.6Cu0.4} \sim 3 \times 10^{-17}$J for the thin films annealed at 450°C. Therefore, the nucleation barrier height in case of non-classical nucleation of fcc $Cr_{0.6}Cu_{0.4}$ precipitate is nearly three orders of magnitude higher than that obtained for the classical nucleation of pure fcc Cu precipitate.

Appendix A3. Calculation of non-classical nucleation barrier for the metastable bcc $Cr_{0.6}Cu_{0.4}$ precipitates

In the following, it will be assumed that $Cr_{0.6}Cu_{0.4}$ precipitates have bcc crystal structure and a coherent interface exists between the Cr(Cu) matrix and the precipitate where both have identical crystal structure (i.e. bcc). Nucleation barrier for bcc $Cr_{0.6}Cu_{0.4}$ precipitates will be calculated and compared with those obtained for the pure fcc Cu and fcc $Cr_{0.6}Cu_{0.4}$ precipitates. At first, chemical driving force for nucleation of bcc $Cr_{0.6}Cu_{0.4}$ precipitates at 450°C has been calculated (using Eq. (A9) in Appendix A.2) as $(\Delta g_n)_{non-classical-bcc\ Cr0.6Cu0.4} = 0.45 \times 10^9$J/m³ which is just slightly less than $(\Delta g_n)_{non-classical-fcc\ Cr0.6Cu0.4}$ (see above). Molar volumes of both fcc and bcc structure of $Cr_{0.6}Cu_{0.4}$ precipitates are assumed to be same. The elastic strain energy density of bcc $Cr_{0.6}Cu_{0.4}$ precipitates coherent with the bcc Cr(Cu) matrix can be estimated using the theory of Eshelby as follows [67].

$$\Delta g_{el-coherent-misfit} = \quad M_{Cr(Cu)} \times \left(\frac{\delta a}{a}\right)^2 \times ((X_\beta - X_\alpha)^2) \tag{A9}$$

where, $\frac{\delta a}{a}$ is the misfit due to lattice parameter mismatch between bcc Cr(Cu) matrix and bcc $Cr_{0.6}Cu_{0.4}$ precipitates. Rest of the symbols has already been defined earlier. The lattice parameter mismatch $\left(\frac{\delta a}{a}\right)$ has been calculated as 0.4% where the lattice parameter of bcc $Cr_{0.6}Cu_{0.4}$ phase is 0.28765 nm and the strain free lattice parameter of the Cr(Cu) matrix with global composition $Cr_{0.8}\ Cu_{0.2}$ is 0.28881 ± 0.00001 nm from Fig. 12(d) corresponding to 450°C. Putting the value of $X_\beta = 0.4$(and $X_\alpha \ll 1$), the elastic strain energy density $(\Delta g_{el-coherent-Non-classical})$ has been calculated as 0.85×10^6J/m³ which is three orders of magnitude smaller than the chemical driving force for non-classical nucleation $(\Delta g_n)_{non-classical-bcc\ Cr0.6Cu0.4}$ of bcc $Cr_{0.6}Cu_{0.4}$ precipitates. Next, energy of the coherent interface between the bcc $Cr_{0.6}Cu_{0.4}$ precipitates and the bcc Cr(Cu) matrix will be calculated using the following equation [44]:

$$\gamma_{bcc\ Cr(Cu)\ coherent-bcc\ Cr0.6Cu0.4} = \varepsilon\left(\frac{(X_\beta - X_\alpha)}{a}\right)^2 \tag{A10}$$

which is the energy of dissimilar first nearest pair interactions and the symbols have their usual meaning. For bcc $Cr_{0.6}Cu_{0.4}$ precipitates, ε has been calculated as 2×10^{-20}J. α, the lattice parameter of the Cr(Cu) matrix is 0.28881 ± 0.00001 nm (see above). Using Eq. (A10), $\gamma_{coherent-bcc\ Cr0.6Cu0.4}$ has been calculated as 0.038 J/m² which is more than one order of magnitude smaller than the incoherent interface energy $(\sim\gamma_{Cr(Cu)-fccCr_{0.6}Cu_{0.4}}\sim0.84J/m^2)$ calculated above. The nucleation barrier height of the bcc $Cr_{0.6}Cu_{0.4}$ precipitates $\Delta f^*_{homo-non-classical-bcc\ Cr0.6Cu0.4}$ has

been calculated as 4.5×10^{-21}J (using Eq. (A4) in Appendix A1), which is four orders of magnitude smaller than that of the fcc $Cr_{0.6}Cu_{0.4}$ precipitate and one order of magnitude smaller than that of the incoherent pure fcc Cu precipitate.

Appendix A4. Calculation of classical nucleation barrier for pure bcc Cu precipitates

In the following, nucleation barrier of pure bcc Cu precipitate (~100% Cu) assumed to be coherent with the bcc Cr(Cu) matrix has been considered employing the classical nucleation theory. In this case, $(\Delta g_n)_{Classical-bcc\,Cu}$ has been calculated as 1.27×10^{10}J/m^3 which is almost same as $(\Delta g_n)_{Classical-fcc\,Cu}$. Interface energy of the coherent interface between pure bcc Cu precipitate and bcc Cr(Cu) matrix is 0.24 J/m^2 (calculated using Eq. (A10) of Appendix A.3) which is one order magnitude higher than $\gamma_{bcc\,Cr\,(Cu)coherent-bcc\,Cr0.6Cu0.4}$ (~ 0.038 J/m^2) and exactly one third of the incoherent interface energy between the pure fcc Cu precipitate and the bcc Cr(Cu) matrix (~ 0.717 J/m^2). Thus the nucleation barrier height for coherent bcc Cu precipitates ($(\Delta f^*)_{homo-classical-bccCu}$) has been calculated as 1.5×10^{-21}J which is 40 times smaller than the nucleation barrier of incoherent fcc Cu precipitate (i. e. $(\Delta f^*)_{homo-classical-fccCu} \sim 6 \times 10^{-20}$J) and three times smaller than that of the bcc $Cr_{0.6}Cu_{0.4}$ precipitate phase ($\Delta f^*_{homo-non-classical-bccCr0.6Cu0.4}$) .

Appendix A.5

Heterogeneous nucleation barrier of fcc Cu precipitates at the columnar GBs of bcc Cr(Cu) matrix

The mathematical expression for the heterogeneous nucleation barrier of the fcc Cu precipitates at the columnar GB in the bcc Cr matrix can be written as follows [67]:

$$(\Delta f^*)_{hetero\,fcc\,Cu@GBs} = \frac{1}{2}(\Delta f^*)_{homo-fcc\,Cu} \times (2 - 3cos\theta + (cos\theta)^3) \tag{A11}$$

where the GB has been assumed as a flat surface between two bcc Cr(Cu) grains and the fcc Cu precipitate is lens shaped in the form of two spherical caps. 'θ' is the half of the lens angle and $cos\theta$ can be expressed as follows:

$$cos\theta = \frac{\gamma_{bcc\,Cr\,matrix-\,GB_{\{amorphousCr\}}} - \gamma_{fcc\,Cu\,precipitate-\,GB_{\{amorphous\,Cr\}}}}{\gamma_{bcc\,Cr\,matrix-fcc\,Cu\,precipitate}} \tag{A12}$$

$\gamma_{bcc\,Cr\,matrix-\,GB_{\{amorphous\,Cr\}}}$ is the interface energy between the crystalline bcc Cr grain and the amorphous GB in the bcc Cr(Cu) matrix (GB has been treated as amorphous phase in the bcc Cr(Cu) matrix). $\gamma_{fcc\,Cu\,precipitate-GB_{\{amorphous\,Cr\}}}$ is the interface energy between the fcc Cu precipitate and the amorphous GB in the bcc Cr(Cu) matrix. $\gamma_{bcc\,Cr\,matrix-fcc\,Cu\,precipitate}$ is the interface energy between bcc Cr matrix and the fcc Cu precipitates. After using the various interface energy values (detailed calculations of each energy expression has not been presented), $cos\theta$ is found to be 0.085 and the expression $(2 - 3cos\theta + (cos\theta)^3)$ has a value of 1.745 in Eq. (A12). Using the magnitude of the homogeneous nucleation barrier of the pure fcc Cu phase ($(\Delta f^*)_{homo-fccCu}$) as 6×10^{-20}J (see Appendix A1), Eq. (A1) yields the magnitude of the heterogeneous nucleation barrier of the fcc Cu precipitates at the columnar GB as 5.2×10^{-20}J.

Heterogeneous nucleation barrier of fcc Cu precipitates on the metastable bcc $Cr_{0.6}Cu_{0.4}$ precipitates

The mathematical expression for the heterogeneous nucleation barrier of the fcc Cu precipitate on a second phase such as bcc $Cr_{0.6}Cu_{0.4}$ precipitate can be written as follows [67]:

$$(\Delta f^*)_{hetero\,fcc\,Cu\,on\,bcc\,Cr0.6Cu0.4\,precipitate} = \frac{1}{4}(\Delta f^*)_{homo-fcc\,Cu} \times (2 - 3cos\theta + (cos\theta)^3) \tag{A13}$$

where the bcc $Cr_{0.6}Cu_{0.4}$ precipitate has been treated as an inclusion with a flat surface. The shape of the nucleating fcc Cu precipitate is a spherical cap or a half lens. Eq. (A13) shows that the nucleation barrier in this case is one half of that of the full lens condition previously stated in equation (A11) in A.5.1. $cos\theta$ can be expressed as follows:

$$cos\theta = \frac{\gamma_{bcc\,Cr\,matrix-bcc\,Cr0.6Cu0.4} - \gamma_{fcc\,Cu\,precipitate-bcc\,Cr0.6Cu0.4}}{\gamma_{bcc\,Cr\,matrix-fcc\,Cu\,precipitate}} \tag{A14}$$

$\gamma_{bcc\,Cr\,matrix-\,bcc\,Cr0.6Cu0.4}$ is the interface energy between the crystalline bcc Cr grain and the flat surface of bcc $Cr_{0.6}Cu_{0.4}$ ($Cr_{0.6}Cu_{0.4}$ has been treated as an inclusion in the bcc Cr(Cu) matrix). $\gamma_{fcc\,Cu\,precipitate-\,bcc\,Cr0.6Cu0.4}$ is the interface energy between the fcc Cu precipitate and the flat surface of bcc $Cr_{0.6}Cu_{0.4}$ bcc Cr(Cu) matrix. $\gamma_{bcc\,Cr\,matrix-fcc\,Cu\,precipitate}$ is the interface energy between bcc Cr matrix and the fcc Cu precipitates. After using the various interface energy values (detailed mathematical calculations of each energy expression has not been presented here), the expression $(2 - 3cos\theta + (cos\theta)^3)$ has a value of 3.9 in Eq. (A14). Using the magnitude of the homogeneous nucleation barrier of the pure fcc Cu phase ($(\Delta f^*)_{homo-fcc\,Cu}$) as 6×10^{-20}J (see Appendix A1), Eq. (A1) yields the magnitude of the heterogeneous nucleation barrier of the fcc Cu precipitates at the metastable bcc $Cr_{0.6}Cu_{0.4}$ precipitate as 5.8×10^{-20}J which is only marginally higher than the heterogeneous nucleation barrier of the fcc Cu precipitates at the columnar GB (5.2×10^{-20}J).

Heterogeneous nucleation barrier of bcc $Cr_{0.6}Cu_{0.4}$ precipitates at the columnar GBs

The mathematical expression for the heterogeneous nucleation barrier of the bcc $Cr_{0.6}Cu_{0.4}$ precipitates at the columnar GB in the bcc Cr matrix can be written as follows [67]:

$$(\Delta f^*)_{hetero\,bcc\,Cr0.6Cu0.4@GBs} = \frac{1}{2}(\Delta f^*)_{homo-bcc\,Cr0.6Cu0.4} \times (2 - 3cos\theta(cos\theta)^3) \tag{A15}$$

where the GB has been assumed as a flat surface between two bcc Cr(Cu) grains and the bcc $Cr_{0.6}Cu_{0.4}$ precipitate is lens shaped in the form of two spherical caps. 'θ' is the half of the lens angle and $cos\theta$ can be expressed as follows:

$$cos\theta = \frac{\gamma_{bcc\ Cr\ matrix-GB_{\{amorphous\ Cr\}}} - \gamma_{bcc\ Cr0.6Cu0.4\ precipitate-GB_{\{amorphous\ Cr\}}}}{\gamma_{bcc\ Cr\ matrix-bcc\ Cr0.6Cu0.4\ precipitate}}$$

(A16)

$\gamma_{bcc\ Cr\ matrix-GB_{\{amorphous\ Cr\}}}$ is the interfacial energy between the crystalline bcc Cr grain and the amorphous GB in the bcc Cr(Cu) matrix (GB has been treated as amorphous phase in the bcc Cr(Cu) matrix). $\gamma_{bcc\ Cr0.6Cu0.4\ precipitate-GB_{\{amorphous\ Cr\}}}$ is the interface energy between the bcc Cr0.6Cu0.4 precipitate and the amorphous GB in the bcc Cr(Cu) matrix. $\gamma_{bcc\ Cr\ matrix-bcc\ Cr0.6Cu0.4\ precipitate}$ is the interface energy between bcc Cr matrix and the bcc Cr0.6Cu0.4 precipitate. After using the various interface energy values (detailed calculations of each energy expression in the numerator has not been presented), $cos\theta$ is found to be 0.526 and the expression $(2 - 3cos\theta + (cos\theta)^3)$ has a value of 0.566. Using the magnitude of the homogeneous nucleation barrier of the pure fcc Cu phase $((\Delta f^*)_{homo-bcc\ Cr0.6Cu0.4\ precipitate})$ as 4.5×10^{-21}J (see Appendix A.3), Eq. (A9) yields the magnitude of the heterogeneous nucleation barrier of the bcc Cr0.6Cu0.4 precipitates at the columnar GB as 1.3×10^{-21}J.

Appendix B. Correlation between Stress, texture and phase decomposition in $Cr_{0.8}Cu_{0.2}$ thin films

In the following, observed phase separation in $Cr_{0.8}Cu_{0.2}$ films during annealing has been correlated with the evolution of stress, crystallographic texture and microstructure in the thin films during annealing. Annealing of the alloy thin film at temperature $\geq 300^oC$, caused various microstructural changes (annihilation of lattice defects, changes in the film microstrain and macrostresses, orientations/orientation distribution of crystallites etc.) which in turn affect the thermodynamic stability of the alloy phase due to the change of total Gibbs free energy of the film. Annealing beyond 350^oC reduces the microstrain (see Fig. 6(b)) due to annihilation of lattice defects in the bcc Cr(Cu) matrix without negligible grain growth in the Cr(Cu) matrix (see Fig. 6(a)). Such reduced microstrain and defect density beyond 350^oC is also associated with an increase in the strength and sharpness of the $\{110\}_{bcc}$ fiber texture of bcc Cr(Cu) matrix (see Section 3.3) due to the enhanced alignment of Cr(Cu) crystallites along the < 110 > crystallographic direction. It may be noted that driving force for observed {110} fiber texture of the bcc Cr(Cu) matrix and {111} fiber texture of fcc Cu(Cr) precipitate phase is the minimization of the total surface energy of the $Cr_{0.8}Cu_{0.2}$ thin film (i.e. {110} planes in bcc Cr and {111} planes in fcc Cu are close packed planes having lowest surface energies). It is plausible that the bcc Cr(Cu) matrix phase and the fcc Cu(Cr) precipitate phase follow the so called Kurdjumov-Sachs (K-S) orientation relationship between them. Earlier such K-S orientation relationship between the bcc Fe matrix phase and the fcc Cu phase was reported during the phase decomposition of Fe-Cu binary alloy [92]. Additionally, annealing of the as-deposited thin film leads to a reduction in the tensile residual macrostress in the film particularly beyond 300^oC and hence the strain energy of the film also reduced beyond 300^oC (see Fig. 13). Interestingly, initial phase decomposition in the annealed $Cr_{0.8}Cu_{0.2}$ thin film took place during 300^oC annealing via the formation of the intermediate bcc precipitate phase. Therefore, as expected thermodynamically, the observed phase decomposition of $Cr_{0.8}Cu_{0.2}$ phase is accompanied by the minimization of both surface free energy and the strain free energy of the $Cr_{0.8}Cu_{0.2}$ thin film which in turn reduces the total Gibbs free energy of the film. Phase decomposition of $Cr_{0.8}Cu_{0.2}$ thin film has been further confirmed from the observed decrease in the strain free lattice parameter of the bcc Cr(Cu) matrix due to Cu depletion from the matrix during precipitation of Cu rich fcc Cu(Cr) phase (see Fig. 12(d)). As indicated earlier that beyond 350^oC, negligible growth of Cr(Cu) crystallites (see Fig. 6(a)) is possibly due to the precipitation of Cu(Cr) phase at the GB adjacent regions which causes grain boundary pinning [78]. In the following, stress evolution due to such microstructural changes in the film during annealing has been discussed.

As described in Section 3.4, as-deposited $Cr_{0.8}Cu_{0.2}$ thin films have high tensile residual stresses (~ 1.5 GPa) which are mainly due to coalescence of islands/atomic clusters and subsequent growth of Cr(Cu) crystallites [36]. Such high residual stresses have been found in Cr-Cu binary alloy thin films with higher Cr content [10] and they are consistent with the low atomic mobility of Cr and the observed columnar microstructure of $Cr_{0.8}Cu_{0.2}$ thin films (Fig. 1) [10]. During annealing a non-monotonic change in the $Cr_{0.8}Cu_{0.2}$ thin film stresses could be mainly due to the following reasons: (i) *Stress generation due to grain growth in the Cr (Cu) matrix*: Grain growth in the nanocrystalline Cr(Cu) matrix causes a net shrinkage of the $Cr_{0.8}Cu_{0.2}$ thin film due to reduction of the GB density in the Cr(Cu) matrix. Since the film is bonded to the substrate, such shrinkage of the $Cr_{0.8}Cu_{0.2}$ film leads to generation of tensile stresses (σ_{GS}) in the thin film. Magnitudes of such stresses have been estimated and they are presented in Table 1 (for calculation, see Appendix C1). Table 1 shows that increase of average size of Cr(Cu) crystallites/grains at 200^oC annealing temperature (shown in Fig. 6(a)) leads to nearly ~ 1.4 GPa tensile stress generation in the $Cr_{0.8}Cu_{0.2}$ thin films. However, at higher annealing temperature ($\geq 300^oC$) formation of precipitate phases (confirmed from XRD results) is likely to prevent the normal grain growth (see Fig. 6(a)) in the nanocrystalline Cr(Cu) matrix especially if Cu(Cr) precipitates are present at the matrix GBs due

Table 1
Stress generation during annealing: effects of grain growth, precipitation and thermal stress (Growth stress in the film: 1.5 GPa).

Annealing Temperature K (^oC)	Thermal stress during heating (GPa) (A)	Thermal stress during cooling (GPa) (B)	Residual thermal stress in the films after cooling (GPa) (C) (= B + A)	Film stress due to grain size change (GPa) (D)	Film stress due to Cu (Cr) precipitation (GPa) inside Cr (Cu) grain (GPa) (E)	Film stress due to Cu (Cr) precipitation at the Cr (Cu) grain boundary (GPa) (F)	Net stress in the films (GPa) (Growth stress + (C+D+E+F))
300 (27)	0	0	0	0	0	Compressive	1.49+F
473 (200)	-0.133	0.133	0	1.36	0	Compressive	2.85+F
573 (300)	-0.209	0.209	0	0.45	1.49	Compressive	3.43+F
623 (350)	-0.248	0.337	0.089	1	1.42	Compressive	4+F
673 (400)	-0.286	0.422	0.136	-0.26	1.4	Compressive	2.77+F
723 (450)	-0.324	1.24	0.916	-1.06	1.3	Compressive	2.65+F

to the so-called GB pinning [78]. Calculated compressive stresses for annealing temperature ≥ 400°C are due to bigger initial grain sizes ($L_o > L$, see Appendix C11) which actually results from the data scatter in Fig. 6(a). (ii) *Generation of thermal stresses in the $Cr_{0.8}Cu_{0.2}$ films due to mismatch of thermal expansion coefficients (TECs) between the film and the substrate:* Table 1 shows the magnitude of thermal stresses generated during heating, during cooling and the net residual thermal stresses in the films after cooling assuming no stress relaxation (see Appendix C2 for calculation method). Up to 300°C annealing temperature, the net stress generation due to thermal stresses in the thin films is zero (see Table 1). However, for annealing temperature ≥ 350°C, due to significant volume of fraction of fcc Cu (Cr) precipitates in the Cr(Cu) matrix, the TECs of the thin films during heating are significantly different than those during cooling. Therefore, the thermal stresses generated during heating significantly differ from those generated during cooling and Table 1 shows significant tensile stress generation for annealing temperature 350°C and above. (iii) *Misfit stresses due to the formation of fcc Cu(Cr) precipitates both inside the bcc Cr(Cu) grains and at the GBs:* Difference between the specific volumes of the precipitate ($V_{fccCu(Cr)}$) and matrix ($V_{bcc Cr(Cu)}$) causes an average linear strain up to 0.4% in the bcc Cr(Cu) matrix and localized formation of fcc Cu (Cr) precipitates causes a net shrinkage of the Cr(Cu) matrix as $V_{fccCu(Cr)}$ is smaller than $V_{bcc Cr (Cu)}$. Therefore, a net tensile stress will be generated in the $Cr_{0.8}Cu_{0.2}$ thin film due to the presence of the rigid substrate. Magnitudes of such tensile stresses have been presented in Table 1 for various annealing temperatures (see Appendix C3). On the other hand, when the Cu (Cr) precipitates form at the GBs of the Cr(Cu) matrix, the matrix expands (as molar volume of the Cu(Cr) precipitate is larger than the molar volume of Cr(Cu) grain boundary) and compressive stresses are generated in the films due to the presence of the substrate. Precise calculation of the magnitude of such compressive stress has not been possible due to the unknown molar volume of the Cr(Cu) GBs. However, it may be noted that Cu(Cr) precipitate formation at the Cr(Cu) grain boundaries (see TEM results, Fig. 9) may inhibit the grain growth in Cr(Cu) matrix which in turn stops the generation of tensile stress due to grain growth at higher annealing temperature beyond 300°C. Hence, compressive misfit stresses generated especially beyond 350°C annealing temperature may be the root cause of the observed reduction of the tensile stresses in the $Cr_{0.8}Cu_{0.2}$ films presented in Fig. 12(c). (iv) *Possible stress relaxation in the $Cr_{0.8}Cu_{0.2}$ thin films:* The last column of Table 1 reports net tensile stress generated in the $Cr_{0.8}Cu_{0.2}$ thin films after cooling assuming no stress relaxation due to plastic deformation processes in the films. Such tensile stresses have been plotted in Fig. 12(c) as a function of annealing temperature along with the experimentally measured stress values obtained after X-ray diffraction stress analysis. Large differences between the measured and theoretically modeled stress values suggest either significant stress relaxation (by thermally activated dislocation glide and /or constrained diffusional creep at elevated temperature (i.e. ≥ 350°C) [93,94]) and/or large compressive stress generation in the thin films during the annealing. Estimation of yield strength of the annealed bcc $Cr_{0.8}Cu_{0.2}$ film (see Appendix C4 for calculation) suggests that mechanism other than the plastic deformation of the thin films may be active which reduces the tensile stresses in the Cr(Cu) matrix during annealing (i.e. compressive misfit stress generation in the Cr (Cu) matrix due to Cu(Cr) precipitation at the Cr(Cu) grain boundaries). Both HAADF and overlay of STEM-EDS map of 450°C annealed film show that a majority of the Cu enriched areas is located at the GBs (see Fig. 9(a) and (c)).

Appendix C

Calculation of tensile stress generation due to grain growth

Tensile stresses generated due to grain growth in the $Cr_{0.8}Cu_{0.2}$ thin films during annealing have been estimated using the following equation [36].

$$\sigma_{GS} = -2M_{Cr(Cu)}\Delta a\left(\frac{1}{L} - \frac{1}{L_o}\right)$$

(A17)

Where $M_{Cr(Cu)}$ is the biaxial modulus of the Cr(Cu) matrix which has been taken as the biaxial modulus of {110} fiber textured Cr phase (~ 333 GPa) [95]. Δa is the excess volume per unit area of the GBs. L_o is the average grain size of the as-deposited thin film and L is the average grain size at a particular annealing temperature.

Calculation of thermal stresses in the $Cr_{0.8}Cu_{0.2}$ thin films

Thermal stresses (σ_{th}) generated in the $Cr_{0.8}Cu_{0.2}$ films during heating and cooling have been calculated using the following equation [36]:

$$\sigma_{th} = -(\alpha_f - \alpha_s)M_{Cr(Cu)}(T - T_o)$$

(A18)

Where α_f and α_s are the linear thermal expansion coefficients (TECs) of the $Cr_{0.8}Cu_{0.2}$ film and the Si substrate respectively. T is the final temperature at which the film is under non-zero thermal stress, T_o is the initial temperature at which the film was under zero thermal stress. For the thin films annealed at 200°C and 300°C, the linear TECs of the film and the substrate used for the stress calculation are $4.9 \times 10^{-6}/K$ (for pure Cr phase [96]), $16.5 \times 10^{-6}/K$ (for pure Cu phase [96]) and $2.6 \times 10^{-6}/K$ (for pure Si phase [96]) respectively. However, at 350°C and higher annealing temperature, XRD shows substantial volume fraction of Cu (Cr) precipitates. Therefore, the TEC of the $Cr_{0.8}Cu_{0.2}$ film has been calculated from the respective TECs of pure Cr and pure Cu phases with their respective volume fractions in the thin films (observed from Fig. 2(b)) using the so-called rule of mixture.

Calculation of misfit stresses in the $Cr_{0.8}Cu_{0.2}$ thin films

Stress generation due to the so-called misfit strain (volumetric) between the bcc Cr(Cu) matrix and the fcc Cu(Cr) precipitates can be estimated using the following equation [36] assuming an *incoherent* interface between the precipitate and the matrix:

$$\sigma_{misfit} = M_{Cr(Cu)} \times \frac{1}{3} \times \frac{V_{fcc Cu(Cr)} - V_{bcc Cr(Cu)}}{V_{bcc Cr(Cu)}}$$

(A19)

The symbols have their usual meaning as already described in Eq. (A2) in Appendix A1. Magnitudes of the specific volumes and the biaxial modulus are described in Appendix A1.

Estimation of shear stress for the activation of dislocation source and film yield strength

Stress relaxation due to plastic deformation at elevated temperature (i.e. ≥ 350°C) can be due to (i) thermally activated dislocation glide; (ii) constrained diffusional creep [93,94]. However, an exact quantification of stress relaxation due to above processes is difficult if not impossible. An attempt has been made to estimate the shear stress (τ) necessary to activate the dislocation source using a formalism proposed by Blanckenhagen et al. [94] which is as follows:

$$\tau = Gb/(L/3) \tag{A20}$$

The value of τ has been estimated as 2.2 GPa using the shear modulus (G) of 115 GPa for bcc Cr [97], the Burgers vector (b) of 0.25 nm for the bcc $Cr_{0.8}Cu_{0.2}$ phase and the crystallite/grain size (L) of 40 nm for the annealed $Cr_{0.8}Cu_{0.2}$ thin film. Therefore, the yield strength (σ_y) of the annealed bcc $Cr_{0.8}Cu_{0.2}$ film may be approximately 6 GPa using the relation $\sigma_y = \tau/m^*$ (m^* is the average Schmid factor, $m^* = 0.363$ for bcc structure [98]). Nevertheless, in the present case, due to the microstructural changes in the film during annealing such as presence of Cu(Cr) precipitates), yield strength in the annealed $Cr_{0.8}Cu_{0.2}$ film may have a different value than that estimated above. It is clear that the estimated value of the yield strength is much higher than both the experimentally observed maximum value of the residual stress (~ 2.4 GPa) and theoretically modeled stress (~ 4 GPa) in the annealed $Cr_{0.8}Cu_{0.2}$ film (see Fig. 12(c)) beyond which the tensile stresses start decreasing. Therefore, in reality, mechanism other than the plastic deformation of the thin films may be active for possible relaxation of tensile stresses in the $Cr_{0.8}Cu_{0.2}$ thin film during annealing.

References

[1] Y. Jin, K. Adachi, T. Takeuchi, H.G. Suzuki, Correlation between the cold-working and aging treatments in a Cu-15 wt Pct Cr in situ composite, Metall. Mater. Trans. A 29 (1998) 2195–2203, https://doi.org/10.1007/s11661-998-0044-y

[2] H.G. Suzuki, T. Takeuchi, K. Mihara, K. Adachi, Y. Jin, Y. Tsubokawa, T.S. Srivatsan, K.A. Kahor (Eds.), Processing and Fabrication of Advanced Materials, VII, TMS, Warrendale, PA, 1998, p. 359.

[3] D. Mcintyre, J.E. Sundgren, J.E. Greene, Growth, structure, and physical properties of single-phase metastable fcc $Cu_{1-x}Cr_x$ solid solutions, J. Appl. Phys. 64 (7) (1988) 3689–3696, https://doi.org/10.1063/1.341412

[4] J.F. Hamman, H. Kippenberg, H. Hassler, H. Schreiner, Siemens Forsch, Entwicklungsber 9 (1980) 210.

[5] D.J. Chakrabarti, D.E. Laughlin, The Cr-Cu (Chromium-Copper) system, Bull. Alloy Phase Diagr. 56–68 (1984) 99–102, https://doi.org/10.1007/BF02868727

[6] C. Michaelsen, C. Gente, R. Bormann, Phase formation and thermodynamics of unstable Cu–Cr alloys, J. Mater. Res. 12 (6) (1997) 1463–1467, https://doi.org/10.1557/JMR.1997.0201

[7] T.D. Shen, C.C. Koch, Formation, solid solution hardening and softening of nanocrystalline solid solutions prepared by mechanical attrition, Acta Mater. 44 (1996) 753–761, https://doi.org/10.1016/1359-6454(95)00178-6

[8] Y. Ogino, T. Yamasaki, S. Muruyama, R. Sakai, Non-equilibrium phases formed by mechanical alloying of Cr-Cu alloys, J. Non-Cryst. Sol. 117/118 (1990) 737–740, https://doi.org/10.1016/0022-3093(90)90634-X

[9] A.G. Dirks, J.J. van Den broek, Metastable solid-solutions in vapor-deposited Cu–Cr, Cu–Mo, and Cu–W thin films, J. Vac. Sci. Technol. A 3 (1985) 2618–2622, https://doi.org/10.1116/1.572799

[10] T.P. Harzer, S. Djaziri, R. Raghavan, G. Dehm, Nanostructure and mechanical behavior of metastable Cu–Cr thin films grown by molecular beam epitaxy, Acta Mater. 83 (2015) 318–332, https://doi.org/10.1016/j.actamat.2014.10.013

[11] J. Kim, D.S. Yee, Structures of co-evaporated copper alloys, Thin Solid Films 128 (1985) 67–78, https://doi.org/10.1016/0040-6090(85)90336-0

[12] S.M. Shin, M.A. Ray, J.M. Rigsbee, J.E. Greene, S.A. Barnett, Growth of metastable $Cu_{1-x}Cr_x$ solid solutions by ion mixing during deposition, J. Vac. Sci. Technol. A 1 (1983) 537–538, https://doi.org/10.1116/1.571926

[13] D. Mcintyre, J.E. Sundgren, J.E. Greene, Metastable face-centered-cubic Cu1–xCrx alloys (0 < x < 0.23) deposited by sputter deposition: growth, structure, and physical properties, J. Vac. Sci. Technol. A 6 (1988) 1708–1709, https://doi.org/10.1116/1.575317

[14] A.P. Payne, B.M. Clemens, Metastable copper-chromium alloy films, J. Mater. Res. 7 (6) (1992) 1370–1376, https://doi.org/10.1557/JMR.1992.1370

[15] R. Raghavan, T.P. Harzer, V. Chawla, S. Djaziri, B. Phillipi, J. Wehrs, J.M. Wheeler, J. Michler, G. Dehm, Comparing small scale plasticity of copper-chromium nanolayered and alloyed thin films at elevated temperatures, Acta Mater. 93 (2015) 175–186, https://doi.org/10.1016/j.actamat.2015.04.008

[16] R. Raghavan, J.M. Wheeler, T.P. Harzer, V. Chawla, S. Djaziri, K. Thomas, B. Phillipi, C. Kirchlechner, B.N. Jaya, J. Wehrs, J. Michler, G. Dehm, Transition from shear to stress-assisted diffusion of copper–chromium nanolayered thin films at elevated temperatures, Acta Mater. 100 (2015) 73–80, https://doi.org/10.1016/j.actamat.2015.08.016

[17] C. Lin, G.W. Yang, Z.F. Li, B.X. Liu, Formation of non-equilibrium alloy phases in Cr–Cu multilayered films by ion mixing, Mater. Lett. 42 (2000) 7–11, https://doi.org/10.1016/S0167-577X(99)00150-0

[18] X. Wang, J. Zhao, J. He, Investigation on the microstructure and mechanical properties of the spray-formed Cu–Cr alloys, Mater. Sci. Eng. A 460–461 (2007) 69–76, https://doi.org/10.1016/j.msea.2007.01.023

[19] J.R. Childress, C.L. Chien, Reentrant magnetic behavior in fcc Co-Cu alloys, Phys. Rev. B 43 (1991) 8089–8093, https://doi.org/10.1103/PhysRevB.43.8089

[20] C. Michaelson, On the structure and homogeneity of solid solutions: the limits of conventional X-ray diffraction, Philos. Mag. A 72 (1995) 813–828, https://doi.org/10.1080/01418619508243802

[21] A.E. Berkowitz, J.R. Mitchell, M.J. Carey, A.P. Young, S. Zhang, F.E. Spada, F.T. Parker, A. Hutten, G. Thomas, Giant magnetoresistance in heterogeneous Cu-Co alloys, Phys. Rev. Lett. 68 (1992) 3745–3748, https://doi.org/10.1103/PhysRevLett.68.3745

[22] A. Tsoukatos, H. Wan, G.C. Hadjipanayis, Microstructure and magnetic hysteresis of Co-Cu films, Nanostruct. Mater. 4 (1994) 49–59, https://doi.org/10.1016/0965-9773(94)90127-9

[23] C. Gente, M. Oehring, R. Bormann, Formation of thermodynamically unstable solid solutions in the Cu-Co system by mechanical alloying, Phys. Rev. B 48 (1993) 13244–13252, https://doi.org/10.1103/PhysRevB.48.13244

[24] B. Cantor, R.W. Cahn, Vapour-quenched Ag-Cu alloys, Scr. Met. 10 (1976) 381–382, https://doi.org/10.1016/0036-9748(76)90156-3

[25] B. Cantor, R.W. Cahn, Metastable alloy phases by co-sputtering, Acta Met. 24 (1976) 845–852, https://doi.org/10.1016/0001-6160(76)90051-1

[26] H.W. Sheng, G. Wilde, E. Ma, The competing crystalline and amorphous solid solutions in the Ag–Cu system, Acta Mater. 50 (2002) 475–488, https://doi.org/10.1016/S1359-6454(01)00374-3

[27] J. Mimault, G.T. Girardeau, P. Goudeau, K. Reklaoui, Evolution Structurale des Solutions Métastables Formées par Co-Evaporation des Eléments Cu et Mo, J. Phys. IV 435 (C3) (1995) 279–284, https://doi.org/10.1051/jp4:1995327

[28] P. Djemia, F. Ganot, P. Moch, V. Branger, P. Goudeau, Brillouin scattering investigation of elastic properties of Cu–Mo solid solution thin films, J. Appl. Phys. 90 (2001) 756–762, https://doi.org/10.1063/1.1378331

[29] C.L. Chien, S.H. Liou, D. Kofalt, W. Yu, T. Egami, Thomas, J. Watson, T.R. McGuire, Magnetic properties of Fe_xCu_{100-x} solid solutions, Phys. Rev. B 33 (1986) 3247–3250, https://doi.org/10.1103/PhysRevB.33.3247

[30] J. Eckert, J.C. Holzer, C.E. Krill III, W.L. Johnson, Mechanically driven alloying and grain size changes in nanocrystalline Fe-Cu powders, J. Appl. Phys. 73 (1993) 2794–2802, https://doi.org/10.1063/1.353055

[31] E. Ma, M. Atzmon, F. Pinkerton, Thermodynamic and magnetic properties of metastable Fe_xCu_{100-x} solid solutions formed by mechanical alloying, J. Appl. Phys. 74 (1993) 955–962, https://doi.org/10.1063/1.354837

[32] C. Aguilar, V. de, P. Martinez, J.M. Palacios, S. Ordonez, O. Pavez, A thermodynamic approach to energy storage on mechanical alloying of the Cu–Cr system, Scr. Mater. 57 (2007) 213–216, https://doi.org/10.1016/j.scriptamat.2007.04.006

[33] S. Mader, Metastable alloy films, J. Vac. Sci. Technol. 2 (1965) 35–41, https://doi.org/10.1116/1.1492396

[34] S. Mader, Phase transformations in thin films, Thin Solid Films 35 (1976) 195–200, https://doi.org/10.1016/0040-6090(76)90256-X

[35] D.W. Hoffman, J.A. Thornton, The compressive stress transition in Al, V, Zr, Nb and W metal films sputtered at low working pressures, Thin Solid Films 45 (1977) 387–396, https://doi.org/10.1016/0040-6090(77)90276-0

[36] M.F. Doerner, W.D. Nix, Stresses and deformation processes in thin films on substrates, Crit. Rev. Solid State Mater. Sci. 14 (3) (1988) 225–268, https://doi.org/10.1080/10408438808243734

[37] D.S. Gardner, H.P. Longworth, P.A. Flinn, Detection of reactions and changes in thin film morphology using stress measurements, J. Vac. Sci. Technol., A 10 (1992) 1441–1441, https://doi.org/10.1063/1.42683

[38] H. Windischmann, Intrinsic stress in sputter-deposited thin films, Crit. Rev. Mater. Sci. 17 (1992) 547–596, https://doi.org/10.1080/10408439208244586

[39] H.I. Aaronson (Ed.), Lecture on the Theory of Phase Transformation. 2nd ed., TMS, Warrendale, PA, 1999.

[40] H.T. Hesemann, P. Mullner, E. Arzt, Stress and texture development during martensitic transformation in cobalt thin films, Scr. Mater. 44 (2001) 25–30, https://doi.org/10.1016/S1359-6462(00)00553-4

[41] J. Chakraborty, U. Welzel, E.J. Mittemeijer, Interdiffusion, phase formation and stress development in Cu–Pd thin-film diffusion couples: interface thermodynamics and mechanisms, J. Appl. Phys. 103 (2008) 1–15, https://doi.org/10.1063/1.2938079

[42] J. Chakraborty, K. Kumar, R. Ranjan, S.G. Chowdhury, S.R. Singh, Thickness-dependent fcc–hcp phase transformation in polycrystalline titanium thin films, Acta Mater. 59 (2011) 2615–2623, https://doi.org/10.1016/j.actamat.2010.12.046

[43] J. Chakraborty, Phase transformation in ultra-thin films, Adv. Mater. Res. 996 (2014) 860–865, https://doi.org/10.4028/www.scientific.net/AMR.996.860

[44] A. Chbihi, X. Sauvage, D. Blavette, Atomic scale investigation of Cr precipitation in copper, Acta Mater. 60 (2012) 4575–4585, https://doi.org/10.1016/j.actamat.2012.01.038

[45] R.O. Williams, Precipitation process in Cu-Cr alloys, Trans. ASM 52 (1960) 530–538.

[46] J. Rezek, Kinetics of precipitate growth in the copper-chromium system, Can. Met. Quart. 8 (1969) 179–182.

[47] R.W. Knights, P. Wilkes, Precipitation of chromium in copper and copper-nickel base alloys, Metall. Trans. 4 (1973) 2389–2393, https://doi.org/10.1007/BF02669380

[48] Y. Komen, J. Rezek, Precipitation at coherency loss in Cu-0.35 wt pct. Cr, Metall. Trans. A 6 (1975) 549–551, https://doi.org/10.1007/BF02658413

[49] A. Guha, Ph.D. Thesis, University of Pittsburgh, 1977.

[50] Z. Rdzawski, Doctoral thesis, Academy of Mining and Metallurgy, Cracow, 1977.

[51] G.C. Weatherly, P. Humble, D. Borland, Precipitation in a Cu-0, 55 wt% Cr alloy, Acta Met. 27 (1979) 1815–1828, https://doi.org/10.1016/0001-6160(79)90072-5

[52] Z. Rdzawski, J. Stobrawa, Structure of coherent chromium precipitates in aged copper alloys, Scr. Metall. 20 (1986) 341–344, https://doi.org/10.1016/0036-9748(86)90154-7

[53] K. Zeng, M. Hamalainen, Thermodynamic analysis of stable and metastable equilibria in the Cu-Cr system, Calphad 19 (1995) 93–104, https://doi.org/10.1016/0364-5916(95)00010-C

[54] M.A. Turchanin, Phase equilibria and thermodynamics of binary copper systems with 3d-metals. III. Copper-chromium system, Powder Metall. Met. Ceram. 45 (2006) 457–467, https://doi.org/10.1007/s11106-006-0106-x

[55] T. Fujii, H. Nakazawa, M. Kato, U. Dahmen, Crystallography and morphology of nanosized Cr particles in a Cu–0.2% Cr alloy, Acta Mater. 48 (2000) 1033–1045, https://doi.org/10.1016/S1359-6454(99)00411-5

[56] A. Cerezo, T.J. Godfrey, G.D.W. Smith, Application of a position-sensitive detector to atom probe microanalysis, Rev. Sci. Instrum. 59 (1988) 862–866, https://doi.org/10.1063/1.1139794

[57] A. Cerezo, P.H. Clifton, M.J. Galtrey, C.J. Humphreys, T.F. Kelly, D.J. Larson, S. Lozano-Perez, A.M. Emmanuelle, A. Rachel, Oliver, G. Sha, K. Thompson, M. Zandbergen, R.L. Alvis, Atom probe tomography today, Mater. Today 10 (2007) 36–42, https://doi.org/10.1016/S1369-7021(07)70306-1

[58] D. Blavette, A. Bostel, J.M. Sarrau, B. Deconihout, A. Menand, An atom probe for three-dimensional tomography, Nature 363 (1993) 432–435, https://doi.org/10.1038/363432a0

[59] K. Thompson, D. Lawrence, D.J. Larson, J.D. Olson, T.F. Kelly, B. Gorman, In situ site-specific specimen preparation for atom probe tomography, Ultramicroscopy 107 (2007) 131–139, https://doi.org/10.1016/j.ultramic.2006.06.008

[60] X' Pert High Score Plus, Profile fitting software, The Netherlands: PANAlytical (formerly Philips), 2006.

[61] PROFIT, Profile fitting software, The Netherlands: PANAlytical (formerly Philips), 1996.

[62] J.I. Langford, R. Delhez, Th.H. de Keijser, E.J. Mittemeijer, Profile analysis for microcrystalline properties by the Fourier and other methods, Aust. J. Phys. 41 (1988) 173–187, https://doi.org/10.1071/PH880173

[63] I.C. Noyan, J.B. Cohen, Residual Stress, Measurement by Diffraction and Interpretation, Springer-Verlag, New York, 1987.

[64] X-ray properties of materials: henke.lbl.gov/cgi-bin/pert_cgi.pl.

[65] U. Welzel, J. Ligot, P. Lamparter, A.C. Vermeulen, E.J. Mittemijer, Stress analysis of polycrystalline thin films and surface regions by X-ray diffraction, J. Appl. Crystallogr. 38 (2005) 1–29, https://doi.org/10.1107/S0021889804029516

[66] J. Chakraborty, K. Kumar, K.S. Mukherjee, S.K. Ray, Stress, texture and microstructure of zirconium thin films probed by X-ray diffraction, Thin Solid Films 516 (2008) 8479–8486, https://doi.org/10.1016/j.tsf.2008.04.096

[67] J.W. Christian, Theory of Transformations in Metals and Alloys: An Advanced Textbook in Physical Metallurgy, 3rd ed., Pergamon Press, Oxford, 2002.

[68] T.P. Harzer, G. Dehm, Stability, phase separation and oxidation of a supersaturated nanocrystalline Cu-33 at% Cr thin film alloy, Thin Solid Films 623 (2017) 48–58, https://doi.org/10.1016/j.tsf.2016.12.048

[69] I. Kaur, W. Gust, L. Kozma, Handbook of Grain and Interphase Boundary Diffusion Data 1 Ziegler Press, Stuttgart, 1989, p. 458, https://doi.org/10.1002/crat.2170251124

[70] K. Hoshino, Y. Iijima, K.-I. Hirano, Diffusion of vanadium, chromium and manganese in copper, Metall. Trans. A 8A (1977) 469–472, https://doi.org/10.1007/BF02661758

[71] O. Fedchenko, S. Protsenko, P. Zukowski, M. Marszalek, Determination of diffusion coefficients in film systems on the basis of Fe/Cr and Cu/Cr, Vacuum 86 (2012) 1934–1938, https://doi.org/10.1016/j.vacuum.2012.03.022

[72] J.W. Cahn, Phase separation by spinodal decomposition in isotropic systems, J. Chem. Phys. 42 (1965) 93–99, https://doi.org/10.1063/1.1695731

[73] J.W. Cahn, Spinodal decomposition, Trans. Met. Soc. AIME 242 (1968) 166–180, https://doi.org/10.1016/0001-6160(61)90182-1

[74] T.P. Harzer, M.J. Duarte, G. Dehm, *In–situ* TEM study of diffusion kinetics and electron irradiation effects on the Cr phase separation of a nanocrystalline Cu–4 at% Cr thin film alloy, J. Alloy. Compd. 695 (2017) 1583–1590, https://doi.org/10.1016/j.jallcom.2016.10.302

[75] I.J. Polmear, Aluminium Alloys-A century of age hardening, Materials Forum, 28 (2004) pp.1–14, Eds.: by J.F. Nie, A.J. Morton and B.C. Muddle.

[76] K. Hono, S.S. Babu, K. Hiraga, R. Okano, T. Sakurai, Atom probe study of early stage phase decomposition in an Al-7.8 at% Li alloy, Acta Met. Mater. 40 (1992) 3027–3034, https://doi.org/10.1016/0956-7151(92)90466-R

[77] K.H. Hardy, Report on precipitation, Prog. Met. Phys. 5 (1954) 143–278, https://doi.org/10.1016/0502-8205(54)90006-4

[78] C.V. Thompson, Grain growth in thin films, Annu. Rev. Mater. Sci. 20 (1990) 245–268, https://doi.org/10.1146/annurev.ms.20.080190.001333

[79] J.F. Nie, D.E. Laughlin, K. Hono (Eds.), Physical Metallurgy, 5th ed., Elsevier, 2014, pp. 2009–2156, https://doi.org/10.1016/B978-0-444-53770-6.00020-4

[80] S. Sheibani, S. Heshmati-Manesh, A. Ataie, A. Caballero, J.M. Criado, Spinodal decomposition and precipitation in Cu–Cr nanocomposite, J. Alloy Compd. 587 (2014) 670–676, https://doi.org/10.1016/j.jallcom.2013.11.019

[81] R. Becker, W. Doering, Kinetische Behandlung der Keimbildung in übersättigten Dämpfern, Ann. Phys. 24 (1935) 719–752, https://doi.org/10.1002/andp.19354160806

[82] D. Turnbul, J.C. Fisher, Rate of nucleation in condensed systems, J. Chem. Phys. 17 (1949) 71–73, https://doi.org/10.1063/1.1747055

[83] D.A. Porter, K.E. Easterling, M.Y. Sherif, Phase Transformation in Metals and Alloys, 3rd ed., CRC Press, Taylor and Francis Group, 2009.

[84] V. Raghavan, Physical Metallurgy: Principle and Practice, 2nd ed., PHI Learning, New Delhi, 2012.

[85] J.W. Cahn, J.E. Hilliard, Free energy of a nonuniform system. I. Interfacial free energy, J. Chem. Phys. 28 (1958) 258–267, https://doi.org/10.1063/1.1744102

[86] J.W. Cahn, J.E. Hilliard, Free energy of a nonuniform system. III. Nucleation in a two-component incompressible fluid, J. Chem. Phys. 31 (1959) 688–699, https://doi.org/10.1063/1.1730447

[87] J.W.P. Schmelzer, Jr Schmelzer, I.J. Gutzow, Reconciling Gibbs and van der Waals: a new approach to nucleation theory, J. Chem. Phys. 112 (2000) 3820–3830, https://doi.org/10.1063/1.481595

[88] J.W.P. Schmelzer, A.R. Gokhman, V.M. Fokin, Dynamics of first-order phase transitions in multicomponent systems: a new theoretical approach, J. Colloid Interface Sci. 272 (2004) 109–133, https://doi.org/10.1016/j.jcis.2003.08.038

[89] T. Philippe, D. Blavette, Nucleation pathway in coherent precipitation, Philos. Mag. 91 (2011) 4606–4622, https://doi.org/10.1080/14786435.2011.616548

[90] H. Li, D. Tian, J. Quinn, Y.S. Li, F. Jona, P.M. Marcus, Low-energy electron diffraction and photoemission study of epitaxial films of Cu on Ag {001}, Phys. Rev. B 43 (1991) 6342–6346, https://doi.org/10.1103/PhysRevB.43.6342

[91] F.R. de Boer, R. Boom, Cohesion in metals, in: A.R. Miedema, A.K. Nissen (Eds.), WCM Mattens, edition, Elsevier Science Publishers, North Holland, Amsterdam, Netherlands, 1988.

[92] R. Monzen, M. Iguchi, Structural changes of 9R copper precipitates in an aged Fe-Cu alloy, Philos. Mag. Lett. 80 (2000) 137–148, https://doi.org/10.1080/095008300176263

[93] D. Weiss, H. Gao, E. Arzt, Constrained diffusional creep in UHV-produced copper thin films, Acta Mater. 49 (2001) 2395–2403, https://doi.org/10.1016/S1359-6454(01)00168-9

[94] B. von Blanckenhagen, P. Gumbsch, E. Arzt, Dislocation sources and the flow stress of polycrystalline thin metal films, Philos. Mag. Lett. 83 (2003) 1–8, https://doi.org/10.1080/0950083021000050287

[95] D. Baral, J.E. Hilliard, J.B. Ketterson, K. Miyano, Determination of the primary elastic constants from thin foils having a strong texture, J. Appl. Phys. 53 (1982) 3552–3559, https://doi.org/10.1063/1.331134

[96] Thermal expansion coefficient of Cr and Si: ⟨https://en.wikipedia.org/wiki/Thermal_expansion_coefficients_of_the_elements⟩ (data_page).

[97] E. A. Brandes and G. B. Brook, Eds., Smithells Metals Reference Book, 7th ed. Chap.-15.

[98] H. Courtney, Thomas, Mechanical Behavior of Materials, McGraw Hill Education, India, 2013, pp. 142–143 ISBN 978-1259027512. OCLC 929663641.